CBPF-NF-008/97

The Discrete Variational Method and its Applications to Large Molecules and Solid-State Systems

*D.E. Ellis and Diana Guenzburger**

Department of Chemistry and Materials Research Center
Northwestern University, Evanston IL 60208, U.S.A.

*Centro Brasileiro de Pesquisas Físicas - CBPF
Rua Dr. Xavier Sigaud, 150
22290-180 - Rio de Janeiro-RJ, Brasil

ABSTRACT

The Discrete Variational method for molecules and clusters (DVM), in the framework of Density Functional theory, is described in detail. The numerical grids utilized, basis functions and potential are discussed, as well as spin-polarization for magnetic systems, total energy and dynamics. The relativistic version of the DV method is also described. Applications to large molecules range from porphyrins, a transition metal complex of thiophene, the circular molecule "ferric wheel" containing ten Fe atoms and other transition metal complexes investigated by fragments. Examples of relativistic calculations are given for 5d-metal complexes. Calculations for solids, represented by embedded clusters as large as 65-75 atoms, include transition metals, perovskites, silicates and rare-earth borocarbides. Properties investigated and analysed are structural, optical, hyperfine, magnetic and superconducting. The electronic structure and chemical bonds are also studied by Mulliken populations and charges, bond order, density of states and spin density maps; results are related to experimentally observed characteristics.

Key-words: Density functional; Electronic structure; Molecules; Solids.

Contents

1 Introduction **3**

2 The Discrete Variational Method for Molecules and Clusters **6**

2.1 General Formulation of the Method 6
2.2 The Three-Dimensional Point Grid 7
  2.2.1 Pseudorandom Scheme 7
  2.2.2 Product Rules 9
  2.2.3 Partitioning Rules 10
2.3 Basis Sets 10
  2.3.1 Generation of NAOs 10
  2.3.2 Symmetry Orbitals 13
  2.3.3 Orthogonalization and Frozen Core 13
2.4 Magnetic Systems 14
2.5 Charges, Configurations and Magnetic Moments 15
  2.5.1 Population Analysis 15
  2.5.2 Volume-resolved Analysis 15
2.6 The Potential 16
  2.6.1 Coulomb Interaction 16
  2.6.2 Exchange and Correlation 18
  2.6.3 External Potential (Embedding) 19
2.7 Total Energy and Structural Properties 19
2.8 Relativistic DVM 21
2.9 DVM as a Subroutine for Dynamics 23
2.10 Summary of the Computer Code 25

3 Molecules **26**

3.1 Porphyrinic Molecules and Solids 26
3.2 [Cp (CO)$_2$ Fe (η^1-T)]$^+$ 29
3.3 The Molecular "Ferric Wheel" 30
3.4 Molecular Fragments 32
3.5 Relativistic Effects in Molecules with 5d-metals 34
  3.5.1 [Ir(CN)$_5$]$^{3-}$ 34
  3.5.2 Metal-cluster Halogen Complexes 34

4 Solids **38**

4.1 Magnetism and Superconductivity in Borocarbides 38

4.2 γ-Fe and γ-Fe/Al Particles in Copper 41

4.3 Annite, A Silicate Mineral 43

4.4 An Electroceramic Grain Boundary 45

References **85**

1 Introduction

For many decades, first principles computational Quantum Chemistry methods were primarily based on Hartree-Fock (HF) theory and HF augmented by various levels of perturbation theory. These methods have served well as tools to study in full detail the spectroscopic and structural properties of small molecules, with perhaps as many as ten light atoms [1],[2]. Much insight has been gained on the relationships between ground state properties, single-electron orbitals and chemical reactions. While the energy-minimization principle defining the HF wavefunction limits the accurracy of excited state descriptions, nevertheless, much useful information has been obtained about excitation properties and spectra. With perturbative treatment of electron correlation, the systems successfully studied have been extended to "average"-sized molecules (10-50 atoms) containing first-row elements such as C, N or O, or smaller molecules containing a transition element of the first period. The development of effective core potentials, in which inner-shell electrons are "frozen" and do not participate in variational relaxation, has permitted the extension of HF methodology to transition metal particles and heavy atom systems [3],[4]. Nevertheless, the computational load rises rapidly with some power (N^3 or N^4 for HF, N^5 or greater for correlation corrections) of the number of basis functions N, with the exchange interaction being the main bottleneck.

Full-scale treatments of correlation effects, found to be necessary to repair some of the known deficiencies of the HF model wavefunction, generally are done by Configuration Interaction theory [1],[5]. With highly developed computer codes it has been found possible to include more than $10^5 - 10^6$ determinants, either explicitly or implicitly in the wavefunction expansion. Unfortunately, procedures for selecting the most important terms in the CI expansion have proved to be a source of difficulty, despite successes of Coupled Cluster methods and related schemes [6],[7].

However, during the last decades we have witnessed a great evolution and development in the synthesis of new and complex molecules. Large molecules with exotic geometries, polynuclear transition-metal complexes, transition-metal planar molecules stacked to form one-dimensional metals, are but a few examples of the challenging structures that can now be prepared. Moreover, the extraordinary advances in material sciences, frequently motivated by technological developments, have increased the relevance of solid-state materials to chemists, with problems such as heterogeneous catalysis, adhesion and other surface phenomena, synthesis of new complex crystals, impurities and defects in solids, etc.

To meet these new challenges, during the last decade Quantum Chemists have turned more and more frequently to first-principles methods based upon Density Functional (DF) theory [8],[9],[10]. Its simplest implementation, the Local Density approximation (LDA) already provides a surprisingly accurate approximation to the many-body interelectronic potential and a relatively fast means to obtain the electronic structure and properties of molecules and solids [11],[12]. More sophisticated approaches, which employ gradients of the electron density in approximating the electronic exchange and correlation have been shown capable of delivering "chemical accuracy" ($2 - 5$ kcal/mole) in atomic binding energies and precision in bond lengths and angles approaching that of experiment [8]-[12].

Since the LDA has been used in the huge majority of published work, we will largely focus on it in the following. We want to emphasize however, that the newer methodologies such as GGA (Generalized Gradient Approximation [13]) provide useful, but relatively small corrections to an essentialy correct picture of electronic structures. One can of course find examples (e.g., the magnetic ground state of bcc iron), where LDA is qualitatively incorrect and so-called nonlocal corrections are essential.

LDA methods have been employed to investigate solids in two types of approaches. If the solid has translational symmetry, as in a pure crystal, Bloch's theorem applies, which states that the one-electron wave function ϕ_n at point $(\vec{r}+\vec{R})$, where $\vec{R}$ is a Bravais lattice vector, is equal to the wave function at point $\vec{r}$ times a phase factor:

$$\phi_n(\vec{r}+\vec{R}) = e^{i\vec{k}.\vec{R}}\phi_n(\vec{r}) \tag{1}$$

Based on this property, LDA band-structure methods were generated [14], in which the electronic energy levels are obtained in the reciprocal $\vec{k}$ space. Since the early 60's, there have been developed a large number of band structure methods, differing among themselves mainly in the way the crystal potential is treated, and in the choice of expansion bases. Frequently they may be recognized in the literature by their initials: APW, LMTO, FLAPW, KKR, etc.

However, if translational symmetry is missing, band-structure calculations are not possible, or else become highly artificial in nature. This includes a number of interesting and important cases such as impurities in solids (substitutional or interstitial), vacancies, local geometry distortions, atoms or molecules on surfaces, disordered materials, etc. For these cases, DF methods in real space may be applied, if one considers a group of atoms (cluster) to represent the solid. In fact, the same methodology as designed for molecules may be applied, with one important difference: an adequate embedding scheme has to be devised, to insert the cluster in its proper environment in the solid.

The Discrete Variational (DV) Method [15],[16] is an all-numerical self-consistent method based on DF theory, in which the one-electron wave-functions of the molecule or the cluster are expanded on a basis of numerical atomic orbitals (NAO), obtained from DF calculations for atoms or ions. These features make the DVM less computer-time consuming than the Gaussian-basis DF counterparts, and thus suitable to treat large molecules and sizable clusters representing solid-state systems. Heavy atoms may also be included, such as transition-metals, lanthanides and actinides. A relativistic version with four-component one-electron functions is also available [17],[18]. For treating clusters, embedding schemes are built in, which include short-range effects of the first neighbors, as well as long-range Coulomb potentials, in the case of charged atoms.

Although most DVM applications so far have been made within the Local Density approximation, non-local corrections to exchange and correlation [13],[19] have been implemented for calculation of dissociation energies and structural properties.

In this review we shall attempt to describe the main features of the DV method in its current form, and give examples of both molecular and cluster calculations, and of the many different properties that may be investigated.

2 The Discrete Variational Method for Molecules and Clusters

2.1 General Formulation of the Method

The purpose of the DV method is to solve self-consistently the set of Kohn-Sham equations [8], [9], [20] (in Hartree atomic units):

$$h_{KS}\phi_i(\vec{r}) \equiv \left[-\nabla^2/2 - \sum_q \frac{Z_q}{|\vec{r}-\vec{R}_q|} + \int \frac{\rho(\vec{r'})}{|\vec{r}-\vec{r'}|} d^3r' + V_{xc}\right] \phi_i(\vec{r}) = e_i\phi_i(\vec{r}) \tag{2}$$

with

$$\rho(\vec{r}) = \sum_i n_i |\phi_i(\vec{r})|^2 \tag{3}$$

where $\phi_i(\vec{r})$ are the one-particle functions for the molecule or the cluster with occupation n_i, and $\rho(\vec{r})$ is the n-representable density. The first term in Eq. (2) is the kinetic energy, the second term is the Coulomb potential of the nuclei V_n, the third term the electronic Coulomb potential V_e and V_{xc} is the exchange and correlation potential. In the DV scheme, the one-electron functions are expanded on a basis of numerical atomic orbitals (NAO), obtained themselves by LDA calculations [14], [21]-[25]

$$\phi_i(\vec{r}) = \sum_\ell \chi_\ell(\vec{r}) c_{\ell i} \tag{4}$$

An error functional Δ_{ij} is defined, related to approximate solutions of Eqs. (2), which is minimized with respect to variations of the coefficients c_{ij} of Eq. (4), on a discrete set of points $\vec{r}_k$ with weight $\omega(\vec{r}_k)$ in three-dimensional space:

$$\Delta_{ij} = \langle\phi_i|h_{KS} - \varepsilon|\phi_j\rangle = \sum_k \omega(\vec{r}_k)\phi_i^*(\vec{r}_k)(h_{KS} - \varepsilon)\phi_j(\vec{r}_k) \tag{5}$$

Substituting (4) in (5), we obtain:

$$\Delta_{ij} = \sum_k \sum_\ell \sum_m \omega(\vec{r}_k)\left[c_{\ell i}^* \chi_\ell^*(\vec{r}_k)(h_{KS} - \varepsilon)\chi_m(\vec{r}_k) c_{mj}\right] \tag{6}$$

To minimize the functional Δ_{ij} with respect to variations of the eigenfunctions ϕ_i, it is required that

$$\frac{\partial \Delta_{ij}}{\partial c_{\ell i}} = 0 \tag{7}$$

for all i, j and ℓ. This procedure results in the secular equations in matrix form, formally identical to those of the analytical Rayleigh-Ritz variational method:

$$([H] - [E][S])[C] = 0 \tag{8}$$

By solving Eqs. (8) self-consistently, the eigenvalues and eigenvectors of the Kohn-Sham operator in Eq. (2) are obtained. In fact, calculating $[C]$ for a given initial h_{KS} leads to a new $\rho(\vec{r})$ through Eqs. (3) and (4), and thus to a new operator, since the potential is a functional of ρ. The matrix elements of the energy matrix $[H]$ and the overlap matrix $[S]$ are summations over the set of the points $\vec{r}_k$:

$$\begin{aligned} H_{\ell m} &= \sum_k \omega(\vec{r}_k)\chi_\ell^*(\vec{r}_k)h_{KS}(\vec{r}_k)\chi_m(\vec{r}_k) \\ S_{\ell m} &= \sum_k \omega(\vec{r}_k)\chi_\ell^*(\vec{r}_k)\chi_m(\vec{r}_k) \end{aligned} \tag{9}$$

More generally, after the self-consistent ρ is obtained, for any operator $\hat{O}$ the expectation value is defined as:

$$\langle \hat{O} \rangle = \sum_k \omega(\vec{r}_k) \sum_i n_i \phi_i^*(\vec{r}_k)\hat{O}\phi_i(\vec{r}_k) \tag{10}$$

2.2 The Three-Dimensional Point Grid

The scheme of sampling, with weights $\omega(\vec{r}_k)$, is quite flexible, allowing concentration of computational effort in regions of greatest interest. It also allows the users to choose the level of precision of results, permitting rapid surveys of general features, as well as precise calculation of sensitive quantities. Three types of sampling schemes have been implemented, which can be used separately or in combination: pseudorandom, product rules, and partitioning rules.

2.2.1 Pseudorandom Scheme

The basic grid of points in three dimensions is generated with the Diophantine method [26]-[28], which is pseudo-random in the sense that the same "random" point distribution is obtained for the same set of initial parameters. This grid is generally adequate for the region between the atoms, where the valence functions dominate and no large variations in the density occur.

In the Diophantine method as originally formulated [26], [27], the integral I of a periodic function of n variables with period L is estimated by the summation:

$$I = \int F(\vec{r})dx_1 \cdots dx_n \cong \frac{1}{N}\sum_{m=1}^{N} F(\vec{r}_m) \tag{11}$$

This summation converges to I as N^{-K}, $K \geq 1$.

The points $\vec{r}_m$ are given by [26]

$$\vec{r}_m = mL\vec{\alpha} \tag{12}$$

where $\vec{\alpha} = (\alpha_1\alpha_2\cdots\alpha_m)$ is a vector with components given by linearly independent irrational numbers.

This method may be adapted for a molecule or crystal, by choosing spherical coordinates centered at each nuclei as integration variables [28]. These may be mapped to periodic variables in the interval [0,1]

$$\begin{aligned} 0 \le r < \infty &\longrightarrow 0 \le \xi < 1 \\ 0 \le \theta < \pi &\longrightarrow 0 \le \nu < 1 \\ 0 \le \phi < 2\pi &\longrightarrow 0 \le \mu < 1 \end{aligned}$$

by the transformations:

$$\begin{aligned} &\xi(r) = \int_0^r r^2 D(r) dr \\ &\theta = arc\ cos(1-2\nu) \\ &\phi = 2\pi\mu \end{aligned} \tag{13}$$

where $D(\vec{r})$ is the Wronskian of the transformation

$$I = \int_0^\infty \int_0^\pi \int_0^{2\pi} \frac{F(\vec{r})}{D(r)} D(r) r^2 sin\theta dr d\theta d\phi = \int_0^1 \int_0^1 \int_0^1 G(\xi,\nu,\mu) d\xi d\nu d\mu \ . \tag{14}$$

We may thus write from Eq. (11):

$$I \cong \frac{1}{N}\sum_{k=1}^{N} G(\xi_k,\nu_k,\mu_k) = \sum_{k=1}^{N} \frac{F(\vec{r}_k)}{ND(\vec{r}_k)} \equiv \sum_{k=1}^{N} \omega(\vec{r}_k) F(\vec{r}_k) \tag{15}$$

It is convenient to define the distribution function $D(r)$ in such a way as to assure a much higher density of points near the nuclei, where the core functions oscillate strongly. This is achieved by defining $D(\vec{r})$ as a summation of Fermi functions centered at the nuclei q:

$$D(\vec{r}) = \sum_q t_q\ d_q(r_q) \tag{16}$$

with

$$d_q(r_q) = \frac{A_q}{4\pi r_q^2 [1 + e^{\alpha_q (r_q - R_0^q)}]}$$

where t_q is the fraction of points assigned to nucleus q and A_q a normalization constant such that

$$\int d_q(r) d^3\vec{r} = 1$$

Parameters α_q and R_o^q are usually chosen as equal to one and to half the interatomic distance, respectively.

In Fig. (1) is shown the mapping of variable r into ξ through the Fermi function; the point distribution is more dense near the nucleus:

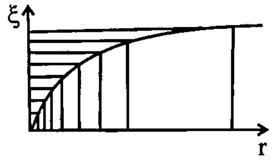

Fig. 1

Finally, the points generated around each nucleus as described above are referred to a common cartesian coordinate system.

If N points are distributed in space according to the distribution function $D(\vec{r})$, then on the average the density of points around a point $\vec{r}$ will be $ND(\vec{r})$. Thus the volume per point around $\vec{r}$ will be

$$\omega(\vec{r}) = 1/(N \times D(\vec{r})) \tag{17}$$

which is the definition of the weight in Eqs. (5), (6), (9) and (10).

2.2.2 Product Rules

The classical product rules of numerical integration [29] are capable of integrating limited regions around an atom to high precision. They are typically of the form of a Gauss-Legendre polynomial rule in (θ, ϕ), multiplied by a radial rule adapted for the asymptotic exponential decay of integrand with distance from the nucleus:

$$\mathrm{w}(\vec{r}_k) = u(\theta_i, \phi_i)\nu(r_j) \tag{18}$$

The angular mesh implemented consists of 6, 12, 24, 32, 50, or 74 points, capable of integrating successively higher order polynomials, or a uniform-area mesh of N^2 points. The radial integration is a modified Simpson's rule in the variable ℓnr, with outer radius r_{max}, number of points, and logarithmic step selected as input.

The scheme is recommended for atomic volumes in which better precision is needed in the core region; e.g. for total energy, hyperfine interactions, and core-level spectroscopy.

2.2.3 Partitioning Rules

The Fermi distributions of the pseudorandom scheme form a set of overlapping atom-centered functions whose density $D(\vec{r})$ provides a sampling scheme with expectation values $\langle O\rangle$ which converge to their integrals. A generalization of this approach can be derived from the long-used *partitioning* methods of X-ray and neutron crystallography. Let

$$D(\vec{r}) = \sum_q t_q d_q(r_q) = 1 \tag{19}$$

where $t_q > 0$ are weights and $d_q(r)$ are selected functions centered on atoms, bonds, points of symmetry, etc. Then the expectation value of $F(\vec{r})$ is given as

$$\langle F\rangle = \langle DF\rangle = \sum_q t_q \langle d_q F\rangle = \sum_q t_q F_q \tag{20}$$

so that each component F_q can be treated independently.

The partitioning functions have been chosen variously as Gaussians, atomic-like densities (proatoms, [30]), and inverse powers of r; the latter is implemented in the DV program. One advantage of this approach, as emphasized by Becke [31], is that classical product rules can be applied to the overlapping multicenter density, to obtain integrals of high precision.

2.3 Basis Sets

2.3.1 Generation of NAOs

As described in Section 2.1, the one-electron functions are expanded on a numerical atomic basis (NAO) (LCAO approximation).

To obtain the basis functions, numerical Local Density calculations are performed for free atoms or ions, employing the same type of exchange-correlation potential as in the molecular (or cluster) calculation (this, of course, is not a necessary condition, but is usually done for the sake of coherence). The atomic self-consistent calculations seek to solve the Kohn-Sham equations on a numerical grid in one-dimension, for an atom with spherical density, such that the atomic orbitals are of the form:

$$\chi_{n\ell} = R_{n\ell}(r)\mathcal{Y}_\ell^m(\theta\phi) \tag{21}$$

where $R_{n\ell}(r)$ are radial functions and $\mathcal{Y}_\ell^m(\theta\phi)$ are real spherical harmonics, which are linear combinations of the usual spherical harmonics Y_ℓ^m.

The grid in the "r" coordinate has a maximum of 300 points, which are distributed according to a logarithmic scale, such that their density is higher near the nucleus.

The LDA radial Schrödinger equation is solved by matching the outward numerical finite-difference solution to an inward-going solution (which vanishes at infinity) of the same energy, near the classical turning point. Continuity of $P_{nl}(r) = rR_{n\ell}(r)$ and its derivative determines the eigenvalue ε_{nl}. The second order differential equation is actually solved as a pair of simultaneous first-order equations, so that the nonrelativistic and relativistic (Dirac equation) procedures appear similar.

One very significant feature of the DV method is thus the flexibility gained by creating the basis functions specifically for a given molecular or cluster calculation, as opposed to methods where "standard" Gaussian basis are employed. This allows one to utilize basis sets of good quality with a considerably smaller number of functions, thus making possible calculations for large systems. There are several ways in which the basis functions may be adapted to some molecule or cluster. One way is to perform a Mulliken population analysis [32], [33] for the atoms in the molecule or cluster, after a first set of iterations is performed. For these preliminary iterations, the basis set is constituted of atomic functions obtained for the free atoms in their ground-state configuration (or free ions, in the case of ionic compounds). The result of the Mulliken analysis after this first self-consistency procedure will give new (fractional) occupation numbers for the atomic orbitals. These occupations, more representative of the situation in the compound, are in turn used to generate new basis functions by atomic self-consistent calculations. Fractional occupation of orbitals is a concept compatible with Density Functional theory. The following schematic representation summarizes this procedure:

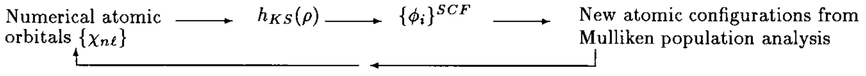

The NAO basis usually contains all the occupied orbitals of the atom, plus some unoccupied level(s) very close in energy. For example, transition metals will include all occupied levels up to nd, $(n+1)s$ and also the virtual level $(n+1)p$. Some additional features make it possible to further improve the basis. If the atom has a negative charge, or if additional virtual orbitals of higher energy are to be included as very diffuse functions, the atomic SCF calculation may be performed in the presence of a "potential well". This well may also be employed when it is desirable to contract the valence atomic basis functions, as is often the case with solids. The well is best described by the following diagram:

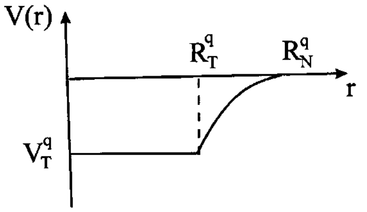

Fig. 2

$$V_A^q = \begin{cases} V^q(r) + V_T^q, & r \le R_T^q \\ V^q(r) + V_T^q.\dfrac{(R_N^q - r)^2 \times (r - \frac{3R_T^q - R_N^q}{2})}{(R_N^q - R_T^q)^3/2}, & R_T^q < r < R_N^q \\ V^q(r), & r \ge R_N^q \end{cases} \tag{22}$$

where V_A^q is the modified atomic potential generating the NAO, $V^q(r)$ is the unmodified atomic potential of atom "q", V_T^q is the depth of the well and R_T^q, R_N^q are truncation distances. The parameters V_T^q, R_T^q and R_N^q depend on the size of the atom and the degree of contraction desired, and their values are dictated by the bonding characteristics of the system.

Sometimes it is inconvenient to use NAOs derived from a specific atomic configuration; e.g., as defined by Mulliken SCF cluster or molecular populations. A marginally better set can be obtained directly from the SCF cluster or molecular *potential*, spherically averaged about each atom site, with an additional well like that of Eq. (22). This NAO basis provides perhaps the most compact and efficient expansion set.

2.3.2 Symmetry Orbitals

For both molecules and clusters, point summetry, if present, is an asset to be exploited. As is known from group theory, the Hamiltonian matrix in the secular equations (Eq. 8) will be separated in smaller blocks which may be diagonalized independently, if the basis used is constituted by functions which transform according to the irreducible representations of the point group of the molecule or cluster. Accordingly, these are obtained previously, utilizing a very general code that can deal with both single and double groups, the latter for relativistic calculations [34], [35]. The non-relativistic symmetrized basis functions are thus of the form:

$$\chi^{\eta}(\vec{r}) = \sum_{q,m} b^{\eta}_{qm} R_{n\ell}(r_q) \mathcal{Y}^{m}_{\ell}(\theta_q \phi_q) \tag{23}$$

where $\eta = (k, \lambda)$ specify the point group irreducible representation and its matrix column, for which the linear combination Eq. (23) forms a basis. Therefore, the linear expansion in Eq. (4) is substituted by:

$$\phi^{\eta}_{i}(\vec{r}) = \sum_{\ell} \chi^{\eta}_{\ell}(\vec{r}) c^{\eta}_{\ell i} \tag{24}$$

and all matrix elements are calculated with the symmetrized basis.

In general, clusters which represent a solid, with or without impurities or defects, may present considerable symmetry if the center of coordinates is placed at a conveniently chosen atom or interstitial site. In the case of one impurity, it is usually advantageous if possible to place it at the center to obtain a point group of higher order. Inorganic molecules and transition-metal complexes also usually have symmetry groups of high order. In the case of large organic molecules, organometallics or biological molecules, symmetry is usually low or nonexistent; this of course will increase the computational time and impose limitations on the size of the basis. On the other hand, of course, organic molecules or organic ligands are usually constituted of small atoms, such as C, N, O, etc. Thus the maximum size of the system that can be treated will depend on a balance among several factors such as number and size of the atoms and symmetry group.

2.3.3 Orthogonalization and Frozen Core

The core orbitals of atoms are those which, by definition, are negligibly modified by the molecular or solid environment. Such orbitals can be excluded from the variational space with a significant improvement in computational time and space. This is accomplished by explicitly orthogonalizing the molecular or cluster valence functions against the core basis functions in the first iteration. In this respect the DV scheme differs from many others, which use parametrized Effective Core Potentials [36] to achieve similar results.

The choice of which orbitals may be "frozen"; i.e., placed in the core, and which should remain in the variational space depends upon properties and precision required. For example, in first-period transition metals it is important to include the 3s, 3p "shallow core" in the variational space when sensitive properties such as the Electric Field Gradient are required. In the process of basis optimization described above, the core orbitals also evolve to become adapted to their environment.

Once the basis functions are obtained, the points of the radial grid around each nucleus where the radial functions $R_{n\ell}(r)$ are defined are interpolated, such that the values of the basis functions are obtained in the three-dimensional grid where the molecular or cluster calculation will be performed.

2.4 Magnetic Systems

In the presence of unpaired electrons, the molecule or solid becomes magnetic. Since the total number of electrons with $s_z = +1/2$ is different from those with $s_z = -1/2$, the exchange interaction, which exists only among electrons with the same spin, will be different for the two sets of electrons, and so will be the exchange-correlation potential V_{xc}. If the density for spin up electrons is allowed to be different from spin down, by allowing the orbitals in Eq. (4) to be different for each spin σ:

$$\phi_i^\sigma(\vec{r}) = \sum_\ell \chi_\ell(\vec{r}) c_{\ell i}^\sigma \tag{25}$$

then the exchange-correlation potential V_{xc} in the Kohn-Sham equations (Eq. 2), which is different for each spin, will indeed generate $\rho_\uparrow(\vec{r}) \neq \rho_\downarrow(\vec{r})$ after self-consistency. This is the basis for the spin-polarized method, through which a spin-density $[\rho_\uparrow(\vec{r}) - \rho_\downarrow(\vec{r})]$ is generated in the three-dimensional grid, being related to magnetic properties such as magnetic moments and hyperfine fields.

In the spin-orbitals of Eq. (25), the spin-dependence appears only in the coefficients $c_{\ell i}^\sigma$, the basis being the same for both spins. Attempts to use spin-polarized functions in the basis are hindered by the resulting linear-dependence problems. A consequence of this is that the polarization of the localized core orbitals is deficient, due to lack of flexibility. For properties in which spin-polarization of the core is important, the latter must be treated in a different manner. We will return to this subject in a later stage.

2.5 Charges, Configurations and Magnetic Moments

2.5.1 Population Analysis

The expansion in the NAO basis allows the analysis of the charge distribution among the atoms according to the Mulliken populations concept [32], which is based on the LCAO coefficients. In the usual Mulliken scheme, the off-diagonal elements of the charge matrix (overlap populations) are divided equally between the corresponding two diagonal elements, i.e., $q_i = \sum_j Q_{ij}$ where q_i's are the atomic occupation numbers and the Q_{ij}'s are the elements of the charge matrix. In the scheme usually adopted with the DVM [33] the off-diagonal charges are divided in proportion to the diagonal elements, i.e., $q_i = \sum_j [2Q_{ii}/(Q_{ii} + Q_{jj})]Q_{ij}$. This scheme is more satisfactory because it minimizes the negative populations that frequently occur for atomic orbitals that take part in molecular orbitals of antibonding character, for example, the $4s$ and $4p$ orbitals of first-row transition elements.

When the system is magnetic and a spin-polarized calculation is performed, the Mulliken-type populations may be used to define magnetic moments:

$$\mu^q = P^q_\uparrow - P^q_\downarrow \tag{26}$$

where μ^q is the total magnetic moment on atom q (in Bohr magnetons), defined as the difference between the spin up and spin down populations P^q_σ.

Mulliken-type populations are a useful tool when it comes to analysing the charge and spin distribution in a molecule or solid. However, one must bear in mind that there is rigorously no such thing as an "atom" in a molecule or in a crystal, and thus such analysis must be viewed somewhat critically. Especially when atomic orbitals are very diffuse, their Mulliken-type populations may not be very realistic. On the other hand, the Mulliken analysis has the advantage that individual atomic orbital occupations may be obtained.

2.5.2 Volume-resolved Analysis

An alternative manner of analysing charge and spin distributions is to divide space in volumes pertaining to each atom and integrating the charge or spin density inside this volume. In the DVM scheme, of course, the integrations are substituted by the summations:

$$C^q = Z - \sum_{k \in WS} \omega(\vec{r}_k)\rho(\vec{r}_k) \tag{27}$$

$$\mu^q = \sum_{k\in WS} \omega(\vec{r}_k)[\rho_\uparrow(\vec{r}_k) - \rho_\downarrow(\vec{r}_k)]$$

where Z is the atomic number, C^q the charge on atom "q", μ_q its spin moment and WS the Wigner-Seitz volume. This last is defined for each atom as the volume enclosed by the planes intersecting at mid-distance the lines joining the atom to its neighbors. Alternatively, spheres with radii proportional to the atomic or ionic radii may be used.

The volume charge and spin-density partitioning, in some instances, may be more realistic than the Mulliken. The simple sampling procedure of Eq. (27) has the disadvantage that only *total* charges or spin moments are extracted. Also, WS or any particular volume partitioning (see Sec. 2.2.3) is as arbitrary as Mulliken analysis, so that convenience and internal consistency provide the best rationale for choosing one method over another. We note that ℓm-projected components of the densities can be extracted by defining the weights in Eq. (27) as $\omega_{k\ell}^{qm}(\vec{r}_k) \cong \omega(\vec{r}_k)\mathcal{Y}_\ell^m(\hat{r}_q)$ where $\hat{r}_q$ are angular coordinates of sample point $\vec{r}_k$, measured with respect to the center of interest, at $\vec{t}_q$. To be more precise, $\omega(\vec{r}_k)$ should form an integration rule, or the projection polynomials $\mathcal{Y}_\ell^m$ should be orthogonalized on the sample mesh $\{\vec{r}_k\}$.

2.6 The Potential

2.6.1 Coulomb Interaction

In calculating matrix elements of the Kohn-Sham Hamiltonian of Eq. (2), the greatest problem is posed by the electronic Coulomb repulsion. To render this term tractable, it is convenient to cast the electron density $\rho(\vec{r})$ in a model form, so as to calculate the potential by one-dimensional integrations. This is accomplished by approximating ρ by a multicenter overlapping multipolar expansion ρ_M [37]:

$$\rho_M = \sum_j d_j \sum_q^{I}{}' \sum_m C_{\ell q}^{\beta m} R_N(r_q) \mathcal{Y}_\ell^m(\theta_q \phi_q) \equiv \sum_j d_j \rho_j(\vec{r}) \qquad (28)$$

Here $j \equiv (I, \ell, \beta, N)$ denotes a symmetry-equivalent set of atoms I (or any group of atoms for which the model density will be the same), a particular partial wave character (ℓ, β) and a particular radial degree of freedom N. The q summation runs over symmetry-equivalent (or selected group) sites, $\mathcal{Y}_\ell^m$ are the real spherical harmonics and $\vec{r}_q = \vec{r} - \vec{t}_q$ is the local coordinate relative to site $\vec{t}_q$. The coefficients $C_{\ell q}^{\beta m}$ are chosen to be those of the totally symmetrical representation of the point group of the molecule or cluster, to reflect the known symmetry of the density, and d_j are coefficients to be determined variationally.

The radial expansion functions are constituted of two groups: in the first group R_N are the spherical atomic densities obtained from the radial functions $R_{n\ell}$ of the basis, and in the second group R_N are radial functions localized in the range $r_N < r_q < r_{N+1}$, chosen to be piecewise parabolic. In general, only a small number of the latter functions are necessary for each (ℓ, β) partner in the fully symmetric representation to converge the potential.

In many applications, the real density has indeed an approximately spherical distribution around each atom; this is the case, for example, of metals and alloys with compact structures. For such systems the first group of R_N functions is already sufficient to represent ρ within a reasonable approximation. For these cases we have simply:

$$\rho_j(\vec{r}) = \sum_{q}^{I}{}' |R_{n\ell}(r_q)|^2 \mathcal{Y}_0^0(\theta_q \phi_q) \tag{29}$$

since combinations of functions of this kind pertaining to the totally symmetric representation will have coefficients equal to unity.

The d_j coefficients are obtained by a least-squares fit to the charge density in the three-dimensional grid:

$$\sum_k w_k[\rho(\vec{r}_k) - \sum_j d_j \rho_j(\vec{r}_k)]^2 \equiv \langle(\rho - \sum_j d_j \rho_j)^2\rangle = \delta \tag{30}$$

where δ is minimized subject to the constraint that ρ_M integrates to the total number of electrons N_e. This condition is incorporated as a Lagrange multiplier and δ is minimized with respect to the coefficients d_j:

$$\left\{ \frac{\partial}{\partial d_i} \left[\langle(\rho - \sum_j d_j \rho_j)^2\rangle + \lambda \sum_j d_j \int \rho_j dv \right] = 0 \right\} \tag{31}$$

The integral sign denotes numerical integration in one dimension (r), which is performed with precision $< 10^{-8}$. Eqs. (31) give the set of equations:

$$\left\{ \sum_j d_j \langle \rho_j \rho_i \rangle - 2\langle \rho \rho_i \rangle + \lambda \int \rho_i dv = 0 \right\} \tag{32}$$

which are solved simultaneously with:

$$\sum_j d_j \int \rho_j dv = N_e \ .$$

Making use of the well-known expansion [38]:

$$\frac{1}{|\vec{r} - \vec{r}'|} = \sum_{\ell=0}^{\infty} \frac{r_<^\ell}{r_>^{\ell+1}} P_\ell(cos\alpha) \tag{33}$$

where $P_\ell(cos\alpha)$ are the Legendre polynomials and $cos\alpha = (\vec{r}.\vec{r}')/rr'$, and of the addition theorem for spherical harmonics, we arrive at the expression for the Coulomb potential $V_C = V_e + V_n$ (electronic and nuclear):

$$V_C(\vec{r}) = \sum_j d_j \sum_q{}' \sum_{m=-\ell}^{+\ell} C_{\ell q}^{\beta m} V_{N\ell m}(\vec{r}_q) - \sum_q \frac{Z_q}{r_q} \tag{34}$$

where:

$$V_{N\ell m}(\vec{r}_q) = \frac{4\pi}{2\ell+1} \mathcal{Y}_\ell^m(\theta_q \phi_q) \left[\int_0^{r_q} R_N(r'_q) \frac{r'^{\ell+2}_q}{r_q^{\ell+1}} dr'_q + \int_{r_q}^{\infty} R_N(r'_q) \frac{r_q^\ell}{r'^{\ell-1}_q} dr'_q \right] \tag{35}$$

In the case where only the first group of (spherical) functions is considered, we have:

$$V_C(\vec{r}) = \sum_j d_j \sum_q{}' 2\sqrt{\pi} \left[\int_0^{r_q} |R_{n\ell}(r'_q)|^2 \frac{r'^2_q}{r_q} dr'_q + \int_{r_q}^{\infty} |R_{n\ell}(r'_q)|^2 r'_q dr'_q \right] - \sum_q \frac{Z_q}{r_q} \tag{36}$$

In the case of a spin-polarized calculation, a similar fit is performed for the spin density $\rho_s = \rho_\uparrow - \rho_\downarrow$.

2.6.2 Exchange and Correlation

The exchange-correlation potential in Eq. (2) is a functional of the electron density and may be cast in the general form:

$$V_{xc}^\sigma = K \rho_\sigma^{1/3} [1 + f_\sigma(\rho_\uparrow, \rho_\downarrow)] \tag{37}$$

In spin-polarized calculations for magnetic systems, V_{xc}^σ will be different for each spin σ. One of the earliest approximations, known as $X\alpha$, included only the first term in Eq. (37) with an empirical parameter X_α [39]:

$$V_{xc}^\sigma = -3X_\alpha(3\rho_\sigma/4\pi)^{1/3} \tag{38}$$

The Kohn-Sham-Gaspar potential derived from density-functional theory has a similar expression for V_{xc}^σ with $X_\alpha = 2/3$, and only took into account exchange [20],[40]. To include correlation, several forms were proposed for f_σ, with parameters obtained from fits to RPA calculations or more accurate Monte Carlo simulations [41] and different spin interpolations. The current version of the DVM code contains altogether nine choices of V_{xc}^σ, the preferred form being the Vosko, Wilk and Nusair [42] parametrization of the Ceperley and Alder Monte Carlo simulations [43].

To give an idea of orders of magnitude, in a typical cluster calculation the Coulomb energy $\langle \rho V_C \rangle$ is of the order of $\geq 10^5$ Hartrees, while the exchange-correlation energy $\langle \rho_\sigma V_{xc}^\sigma \rangle$ is one order of magnitude smaller. The correlation corrections associated with f_σ are one order of magnitude further reduced.

2.6.3 External Potential (Embedding)

In the case of clusters representing a solid, to the cluster density (and model density) are added the densities of several shells of neighboring external atoms at the crystal sites:

$$\rho = \rho_{\text{cluster}} + \rho_{\text{host}} \tag{39}$$

with

$$\rho_{\text{cluster}} = \sum_{i,\sigma} n_{i\sigma} |\phi_{i\sigma}|^2$$

and

$$\rho_{\text{host}} = \sum_q{}' \rho_q(r_q) \ .$$

This constitutes a critical portion of the embedding scheme, leading to what may be called Potential Embedding. The prime in the summation denotes exclusion of the cluster atoms. The external densities are obtained by LDA atomic calculations. To avoid the spurious migration of the cluster electrons towards the external atoms, the attractive potential of the latter is truncated at a certain value, to simulate the Pauli exclusion principle. Typical truncation is at -0.2 hartrees relative to the Fermi energy E_F, with a range of $2.2 - 2.5$ a.u. from each atomic nucleus.

As is done with the basis, the embedding may be improved by generating external atomic densities for atoms with the configurations that they have in the cluster, as obtained by the Mulliken population analysis:

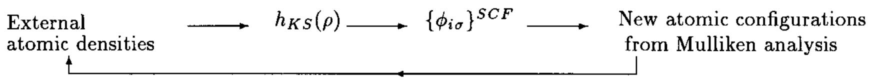

For the case of ionic solids, the method of Ewald summations [44] is employed to take into account the long-range Coulomb potential of the crystal (Madelung potential).

2.7 Total Energy and Structural Properties

Once the self-consistent electron density is obtained for the molecule or cluster, it may be used to calculate the total energy and derived properties, such as dissociation energies, equilibrium interatomic distances, vibration frequencies, etc. Generalizing for a spin-polarized calculation, the expression given by local density theory for the total energy E_t is [8], [9], [20]:

$$E_t = \sum_{k,\sigma} e_{k,\sigma} n_{k,\sigma} + \sum_{\sigma} \int \rho_\sigma \left(-\frac{1}{2} V_e - V_{xc,\sigma} + \varepsilon_{xc} \right) d^3r + \frac{1}{2} {\sum_{pq}}' \frac{Z_p Z_q}{r_{pq}} \tag{40}$$

where $e_{k,\sigma}$ are the Kohn-Sham eigenvalues of Eq. (2), $V_{xc,\sigma}$ is the exchange-correlation potential also known as chemical potential, ρ_σ the model charge density for spin σ as defined in Section 2.6 and V_e the electronic Coulomb potential. The prime in the summation is to leave out self-interaction among the nuclei, and ε_{xc} is the exchange-correlation energy density:

$$E_{xc}[\rho] = \int \rho \varepsilon_{xc}(\rho) d^3r \tag{41}$$

It has been demonstrated [45] that when the density employed in Eq. (40) is the model density ρ_M, as described in section 2.6, the total energy is stationary with respect to variations in ρ_M. In the DV numerical sampling procedure, a scheme is devised to control numerical error, derived mainly from the core region of the atoms, where the wave functions oscillate strongly [45]-[48]. The total energy associated with a volume Ω with nuclei at positions $\{\vec{R}_q\}$ is defined as the expectation value (sum over integration mesh) of the energy density $\varepsilon(\vec{r}, \{\vec{R}_q\})$ over the volume. In order to cancel numerical errors, the computation of E_Ω is made via point-by-point subtraction of a reference system of *noninteracting* (NI) atoms located at the atomic nuclei of a molecule, or at the cluster and embedding atomic nuclei in the case of a solid:

$$E_\Omega = \langle \varepsilon(\vec{r}, \{\vec{R}_q\}) - \varepsilon^{NI}(\vec{r}, \{\vec{R}_q\}) \rangle_\Omega + E_\Omega^{NI} \tag{42}$$

where $\langle\ \rangle$ denote summation in the numerical grid.

The energy density may be defined conveniently as:

$$\varepsilon(\vec{r}, \{\vec{R}_q\}) = \sum_\sigma \left[\rho_{e,\sigma}(\vec{r}) - \frac{1}{2} \left[\rho_\sigma(\vec{r}) + {\sum_q}' Z_q \delta(\vec{r} - \vec{R}_q) \right] V_C(\vec{r}) + \rho_\sigma(\vec{r}) \left[\varepsilon_{xc}(\vec{r}) - V_{xc,\sigma}(\vec{r}) \right] \right] \tag{43}$$

where the single-particle energy is:

$$\rho_{e,\sigma}(\vec{r}) = \sum_i n_{i\sigma} e_{i\sigma} |\phi_{i\sigma}(\vec{r})|^2 \tag{44}$$

and is partitioned into atom-localized contributions in a manner similar to Eq. (28). This step introduces no error, since the partitioning is constructed so as to leave the total (integral) single-particle energy invariant. The sum and δ function in Eq. (43) restrict the nuclear contribution to sites within the integration volume. The prime in the summation leaves out self-interaction of the nuclei. The least-squares determined model density is employed, consistent with the SCF procedure.

In practice, the densities of the non-interacting atoms is obtained from the functions in the NAO basis, to assure maximum error cancellation. When calculating dissociation energies (in molecules) or cohesive energies (in solids), the energy difference between the free atoms and the atoms in the basis, E(free atoms)–E(NI), must be taken into account.

As mentioned in the Introduction, non-local corrections to the LDA total energy of Eq. (40) have been implemented. It has been found that *gradient*-corrected exchange and correlation energies make significant improvements in bond energies and bond lengths. Very little additional improvement is found upon inclusion in the SCF procedure. The simple formula suggested by Becke [19] for exchange correction,

$$\Delta E_x = -\beta \sum_{\sigma} \int \rho_\sigma^{4/3} \frac{x_\sigma^2}{(1 + 6\beta x_\sigma sinh^{-1} x_\sigma)} d^3r \tag{45}$$

with $x_\sigma = |\nabla \rho_\sigma| / \rho_\sigma^{4/3}$ and $\beta = 0.0042$ a.u., has found wide use, and was followed here. The gradient formula developed by Perdew [13] for correlation correction,

$$\Delta E_c = \int d^{-1} e^{-\Phi} C \frac{|\nabla \rho|^2}{\rho^{4/3}} d^3r \tag{46}$$

was chosen, with C, Φ and d being given functions of ρ and ρ_σ. The sum

$$\Delta E_{xc} = \Delta E_x + \Delta E_c \tag{47}$$

may be added to Eqs. (40) and (41) for improved accuracy. Of course, it is the (smaller) difference between molecule and free atoms ΔE_{xc}(molecule) – ΔE_{xc}(free atoms) which enters into structural properties.

2.8 Relativistic DVM

In the preceeding sections we have discussed the DV scheme as it has been applied in nonrelativistic DF theory; here we extend the discussion to solutions of the relativistic Dirac equation,

$$(c\boldsymbol{\alpha} \cdot \vec{p} + mc^2 \boldsymbol{\beta} + V(\vec{r}) - \varepsilon_i)\Psi_i(\vec{r}, \xi) = 0 \tag{48}$$

Here $\boldsymbol{\alpha}$ and $\boldsymbol{\beta}$ are 4×4 matrix operators composed from the Pauli spin matrices, $c = 137.037$ is the speed of light in a.u. and $V(\vec{r})$ is an approximation to the potential seen by an electron with (space, spin) coordinates $(\vec{r}, \xi)$. The one-electron wavefunction Ψ_i are 4-vectors composed of the so-called large and small components of mixed spin, as described in standard texts [49]. The development of suitable potentials V has an extensive literature both in the context of Dirac-Fock theory [50] and Density Functional theory [51]. The principal unresolved problem is that the Coulomb potential as normally written is not Lorentz invariant, and partial solutions such as the Breit interaction and their DF counterparts [52] have not been established as leading to significant improvements in predicted properties. In general it seems that corrections to the commonly used nonrelativistic DF potentials are important essentially for core orbitals, and for the wavefunction structure close to the nucleus [53]. In the following we will assume that the potential V is constructed by the same procedure as in the nonrelativistic case, however, making use of the relativistic density, again defined as in Eq. (3). This methodology has been found to yield quantitatively useful results, in band structure [54], molecules and clusters [17], [55]. The primary differences between nonrelativistic (NR) and relativistic (R) potentials are readily seen in atomic calculations [56]:

1. In the *direct* effects, the s and $p_{1/2}$ shells contract and gain binding energy, due to the kinetic energy operator.
2. The *spin-orbit* interaction partially lifts the degeneracy of the (n, l) shells, leading to states characterized by (n, l, j) with total angular momentum $\mathbf{j}$.
3. In the *indirect* effects, the d and f shells react to the increased nuclear screening and expand, altering the ground state configuration significantly for the heavy metals.

These features carry over into molecules and solids, but are generally more subtle due to the mixing between AOs of different character on different sites.

Since we are interested in magnetic interactions and frequently encounter open-shell systems, an analog of the convenient nonrelativistic spin-polarized scheme is needed. Fortunately, the well-known two-fold Kramer's degeneracy of relativistic wavefunctions, related to time-reversal symmetry, provides a simple solution. We have thus introduced the so-called *moment-polarized* scheme in which functions Ψ_i and $\tau\Psi_i$, where τ is the time-reversal operator, are analogous to the up- and down-spin nonrelativistic spin-orbitals [53, 57]. In atoms, these functions consist of $+m_j$, $-m_j$ components of the (n, l, j) shells and in the absence of a magnetic field are easily shown to be degenerate. External magnetic fields or internal (exchange) fields lift the degeneracy in exactly the same fashion as for up- and down-spin states, and in fact the orbitals are identical for $\ell = 0$ (s-states).

As in the spin-polarized NR case, the convenience of having only two potentials to represent magnetic interactions is obtained at a price. This price includes some contamination of the SCF solutions with a mixture of multiplets, which can sometimes be resolved by projection techniques, including for example, the Slater Sum Rule of atomic theory. The ease of calculation of an R potential which treats exchange in open-shell heavy atom systems reasonably well, without introducing artificial (and incorrect) spin-polarization is a considerable advantage.

Symmetry is also easily exploited in the relativistic case, making use of the double groups and projection operator techniques [58]. A general numerical procedure has been incorporated in the DV codes to generate 4-component NAO symmetry orbitals for all relativistic point groups [34], [35]. The resulting SCF equations and procedures are identical to those of the nonrelativistic case, except that in general matrix elements and wavefunctions are complex numbers. Standard techniques for finding eigenvalues and eigenvectors of Hermitean matrices are used to solve Eq. (8) [59]. As a practical matter, we observe that SCF solutions of the Dirac equation take about twice as much computer time as for the nonrelativistic problem, in a typical application.

2.9 DVM as a Subroutine for Dynamics

In many materials problems, for example at surfaces or interfaces, the chemical composition and nuclear coordinates are not fully known. Indeed, any information which can be obtained by theory on these basic structural properties will be useful, in conjunction with experiment. Spatially Resolved Electron Energy Loss Spectroscopy (SREELS), X-ray near-edge absorption (XANES) and emission, Mössbauer spectra, etc. provide site-specific probes which can be combined with theory to help resolve structures.

In principle, DF calculations can not only provide total energies versus geometry, but also atomic forces [60]. The DF equivalent of the Hellman-Feynman theorem, augmented by contributions due to incomplete basis sets, does indeed provide a viable scheme for molecules and systems with relatively high symmetry [61]. Various methodologies, including gradient-based steepest descent, variable metric, [62] and pseudo-dynamical simulated annealing [63] provide strategies for locating the equilibrium geometry. However, in complex systems; e.g., a metal particle of tens or hundreds of atoms, a stacked-molecular polymer or a grain boundary in a ceramic, there are simply too many degrees of freedom to be attacked in a single quantum calculation. More importantly, there are typically an enormous number of local minima and even physically important transient and metastable states which play a role in the observed spectra and thermodynamic properties.

We have chosen to break the problem into two parts:

1. Use parametrized interatomic potentials to sample the geometry, using classical Molecular Dynamics (MD) or Monte Carlo/Generalized Simulated Annealing (MC/GSA).
2. Take snapshots of the electronic structure at selected geometries and/or time intervals, with DF methods
3. Use the electronic structures calculated to refine the interatomic potentials
4. Project physical properties from a characteristic set of states, and form thermal and/or spatial averages for comparison with experiment.

The MD and MC classical methods are well described in the literature [64] for defects, interfaces and grain boundaries, an embedding scheme is used to focus computational effort on the region of interest [65], [66]. The MD scheme is most useful to extract thermodynamic averages, vibrational data, and to observe evolution of the model system from a selected initial state. On the other hand, the MC/GSA schemes give the option to sample the *entire* parameter space (with sufficient patience) and map out the multiple basins of the potential surface. Of course the results are totally dependent upon the input potentials; thus it is critical to be able to verify and improve their parametrization. In simple molecules and bulk systems this can be done by direct reference to experimental bond lengths, bond angles, cohesives energies, sublimation energies, etc. For example, the GROMOS data base [67] provides a very useful parametrization of a large number of molecular interactions (Hook's law, van der Waals, bilinear angular terms, Coulomb), which can be easily updated. For metals, two body potentials of the van der Waals type and many-body interactions such as the Embedded Atom Method [68] (EAM) and its extensions have found much use and are readily executed. For ionic solids, particularly the oxides, a considerable literature exists, ranging from two-body potentials of the Buckingham type to shell-model potentials which include some aspects of electronic polarization and embedding [69].

In complex systems, particularly with defects and interfaces, experimental data are almost never availabe in sufficient detail to determine the interatomic potentials. Thus theory has an indespensible role in verifying and improving the potential data. We have therefore constructed a hybrid MD/MC-DV procedure which implements classical and quantum aspects just described into a coupled sequence of steps [70]. Without exaggeration, we may call this a "Theorist's Scanning Microscope", as it surveys spatial and temporal characteristics of a system much as an experimental scanning microscope does.

2.10 Summary of the Computer Code

As described in the earlier sections, the DV method is entirely numerical, and thus all variables are defined in the three-dimensional grid. The fundamental characteristic of the architecture of the DVM system of codes is that procedures are executed in the memory for a block of grid points at a time. The blocks of points are created and stored in temporary disk space, from where they are recalled. All variables are calculated and stored in disk for the same blocks. In the current version, blocks of 600 points are used. For the larger calculations, typically $1.0 - 1.5$Gb of temporary disk space must be reserved for this purpose.

A short summary of a SCF calculation is as follows:

1. The program reads in data for the atoms in the cluster, such as Z values and nuclear coordinates, and other parameters.

   A symmetry program determines the point group and generates the coefficients of the symmetry functions for the irreducible representations. This program is entirely general, and works also with the double groups related to the relativistic calculations.

2. The basis functions are generated by local density atomic calculations.

3. The crystal atoms (in the case of solids) are generated at the exterior sites to produce the embedding.

4. The three-dimensional points grid is generated by the Diophantine procedure and/or more accurate schemes. Basis functions, densities, etc., are obtained on the grid points.

5. An initial model charge density ρ_M is constructed by superposing the atomic densities of the basis atoms.

6. The matrix elements are obtained for the matrices in Eq. (8), which are solved by diagonalizing $[H]$. The set of eigenvectors obtained determines a density ρ according to Eq. (3).

7. A new ρ_M is obtained by least-squares fitting the ρ obtained to the expansion in Eq. (28), carried to the desired degree of accuracy.

8. A new model Coulomb potential is obtained according to Eq. (36). Steps (6)-(8) are repeated until the desired degree of self-consistency is reached.
9. When self-consistency is achieved, the related eigenvalues and ρ are stored in a permanent disk file, for further use in calculations of total energy and several other properties.

Finally, it is interesting to emphasize some advantageous features of the DV method:

a) Any operator may be added to the Kohn-Sham hamiltonian, in a simple and straightforward manner, as for example $\vec{E}_0.\vec{r}$ where $\vec{E}_0$ is an external electric field (Stark effect) and $s_z H_0$ (Zeeman effect) where H_0 is an external magnetic field.

b) The usual and most convenient basis sets employed are numerical; however, one may use analytical basis functions such as Slater or Gaussian if desired, simply by tabulating their values in the grid points.

c) A preliminary evaluation of a given physical or chemical system may be done with little computational effort, using few points in the numerical integration grid and less accurate model density.

d) Practically, we observe that the numerical DV scheme scales computationally with the number of basis functions N as N^2, whereas DF methods with Gaussian basis sets scale as N^3, Hartree-Fock as N^4 and GVB or many-body perturbation at the MP2 level as N^5 or higher.

e) In the solution of the secular equations, considerable point-by-point cancellation of numerical errors is achieved.

f) The numerical LDA atomic calculations generate conveniently compact and environment-adapted basis with a small number of functions.

3 Molecules

3.1 Porphyrinic Molecules and Solids

The porphyrins and their derivatives, such as the tetraazaporphines, continue to exhibit a rich chemistry due to varied possibilities of metal and ligand substitution. They appear in an enourmous variety of settings, from industrially important dyes, to biological and water-soluble catalysts, to molecular metals, to model one-dimensional magnetic systems. Gross features of the electronic structure are dominated by the "core", consisting of a divalent metal like Mg or Cu (or H_2) in square planar coordination to C or N ligands. Properties are "tuned" by choice of core elements, and by substitution of peripheral ligands at the outer carbon "fence", see Fig. 3.

From the point of view of transport and low-lying optical excitations, a principal point of interest is the competition between ring-based p_π orbitals and metal-centered orbitals, particularly transition metal 3d orbitals. The balance between, and admixture of, these two components can be modified and thus leads to a varied electrical conductivity and magnetic coupling among elements in the stacked metal conductors based on the monomer porphyrinic building blocks. The partially oxidized metal phthalocyanines, like Cu(Pc)I and $Cu_{1-x}Ni_x$(Pc)I provide a fascinating class of materials with a complex temperature dependence of conductivity and magnetic susceptibility. As more highly purified materials have become available, their intrinsic properties are becoming apparent, and permit systematic properties design based upon doping and substitution strategies [71].

These molecules show strong characteristic electronic absorption in the visible region (Q-band, ca. 680 nm) and UV (Soret or B-band, a broad band with peak ~ 330 nm), with band-splitting and shifts linked to overall symmetry and composition of the macrocycles. Synthesis of molecules with peripherally fused-benzo rings (PC) and dithiolene groups (PZ) permits a detailed analysis of the role of peripheral ligands. A single Q-band peak is observed for 4PZ and 4PC high symmetry (D_{4h}) macrocycles. Ligand substitution leads to the splitting of the Q-band into two peaks in the lower symmetry 2PC/2 PZ cis, 3 PC/1 PZ, 1 PC/3 PZ (C_{2v}) and 2 PC/2 PZ trans (D_{2h}) configurations. Intensities and band splittings and shifts calculated in the DV framework have been compared in detail with qualitative molecular orbital models and experiment in the visible and UV [72].

The partial density of states (PDOS) provides a convenient analysis of wavefunction composition versus energy, making use of the Mulliken population analysis of individual orbitals. Here PDOS is defined as

$$D^q_{n\ell}(E) = \sum_p P^q_{n\ell,p} L(E - e_p, \delta) \tag{49}$$

where $P^q_{n\ell,p}$ is the population of atomic orbital $(n\ell)$ on site q in energy level p, and $L(E - e_p, \delta)$ is a line-shape function with width δ. We typically use a Lorentzian, with $\delta \sim 0.1$ eV for this purpose. A typical PDOS, for the high symmetry 4PZ Ni tetraazaporphyrazine (TAP) case, is shown in Fig. 4.

Here are shown the total DOS and important Ni, C, N and S ligand contributions; an extensive mixing of orbital character in the valence bands is evident. The pinning of the Ni 3d band around the Fermi energy E_F is characteristic of an open shell atom. Unlike the magnetic (S=1/2) copper analogs, the Ni-based compounds are experimentally diamagnetic, as confirmed by the calculations. The mixed $Cu_{1-x}Ni_x$ stacked compounds provide an interesting example of magnetically diluted one-dimensional interactions, whose properties are still being investigated.

Dipole-allowed optical transitions are described in the one-electron DF model in the usual way, with absorption intensity given by

$$I(e) = \sum_{i,f} L(e - e_{if}, \delta) n_i (1 - n_f) f(e_{if}) \tag{50}$$

with $e_{if} = e_f - e_i$, and oscillator strengths f,

$$f(e_{if}, \hat{e}) = \frac{2m}{h^2}\, e_{if}\, |\langle \phi_f | \vec{r} \cdot \hat{e} | \phi_i \rangle|^2 \tag{51}$$

Theoretical and experimental absorption bands of 4PZ Ni (TAP) are given in Fig. 5. The theoretical bands were calculated using the *ground state* wavefunctions; the low-lying Q-band is seen to be in excellent agreement with experiment. The B-band region which marks the onset of strong UV absorption, typically associated with charge-transfer transitions, is fairly well represented. The W-band, centered at ~ 2.5 eV in experiment and attributed to S-based transitions, is considerably blue shifted in the calculations. This may be due in part to substitution by hydrogens in the calculations for terminal groups far away from the porphyrazine ring (-$(CH_2CH_2O)_3H$ in star-porphyrazine and –$(CH_2)_7CH_3$ in the phthalocyanine macrocycle) which are attached to the outer oxygen atoms. In order to test effects of H termination, calculations were also performed using methyl groups as terminators in several cases. No significant differences in *occupied region* electronic structure were found; however, perturbation of the excited state region could occur. Some aspects of electronic relaxation effects on optical transitions were explored, by use of the Transition State (TS) scheme [39]. This approach gives a reasonably good account of excitation energies, when the nuclear framework does not shift significantly between ground and excited states. TS calculations on the Q-band showed shifts of a few tenths eV from one compound to the other, but made no significant overall improvement in the comparison of experiment and theory. TS studies were not made on the higher energy W- and B-band regions; here the effects of electronic rearrangement in the excited state are expected to be greater, and merit further study.

Finally, we touch upon recent work on intermolecular interactions in stacked chain systems, concentrating on Cu(Pc)I. In undoped Cu(Pc), the monomers stack in a slipped herringbone pattern; in the partially oxidized Cu(Pc)I the stacking is vertical. In the latter case, the interplanar spacing is observed as $\Delta Z = 3.19\AA$ with a staggered configuration: each molecule is rotated $\Delta\theta = 42^0$ about the stacking axis with respect to its neighbor below. These values are typical for a wide range of compounds.

MD/MC simulations on dimers and tetramers, using only van der Waals interactions from a standard molecular data base reproduce these features surprisingly well, with predicted values of $\Delta Z = 3.20\AA$ and $\Delta\theta = 45^0$. DF calculations made on the dimer produce very similar results, with the advantage that the angle and distance dependent energy $E_{bind}(z,\theta)$ provides a basis for refinement of the semiempirical potential parameters [70]. An interesting interpretation of the mechanisms of electronic repulsion which favor the staggered ground state configuration was given by Rosa and Baerends [73]. The antiferromagnetic (AF) alignment of Cu moments in the dimer was found to be the ground state, in agreement with the observed AF properties of the solid. This represents a short-range order of the one-dimensional chains; the observed bulk ordering at 4K is believed to be due to three-dimensional interactions among the chains.

3.2 [Cp $(CO)_2$ Fe (η^1-T)$]^+$

A subject of technological interest is the bond between thiophene and a transition metal M. This is due to the hydrodesulfurization of petroleum, which is performed in the presence of a transition metal catalyst [74]

$$C_xH_yS + nH_2 \overset{cat}{\rightarrow} \text{hydrocarbons} + H_2S$$

Thiophene is the compound present in petroleum from which it is most difficult to remove the sulphur, due to this atom begin part of an aromatic ring.

One of the modes of coordination of thiophene to catalyst surfaces most frequently suggested is the S or η^1, in which the bond is formed directly between the sulphur and a transition metal atom. In examples of the S-bonding mode which have been well-characterized by X-ray diffraction, a pyramidal geometry has been found [75], which is also present in the absorption of thiophene on metallic surfaces such as copper [76].

To investigate the bond between thiophene and M in the S (or η^1) mode, DV calculations were performed for the complex ion [Cp $(CO)_2$Fe (η^1 -T)$]^+$ (Cp=cyclopentadienyl, T=thiophene) [77]. Due to the strong covalency between the Fe and the ligands, the electron configuration is a low-spin closed-shell, so that no spin-polarization is present.

Total energy calculations were performed for several values of the angle θ between the plane of the thiophene and the Fe-S bond (see Fig. 6), to determine the equilibrium value. Two minima were revealed, one at 120^0 (deeper) and the other at $\sim 210^0$ (see Fig. 7). An analysis of the changes in the orbitals brought about by the angular variation reveals that the mechanism leading to $\theta < 180^0$ is the reduction of the antibonding interaction between the occupied Fe d_π orbitals and the S π canonical lone pair in free thiophene. This mechanism is consistent with the idea of $sp^2 \rightarrow sp^3$ rehybridization of the S atom in thiophene, which explains the pyramidal geometry.

3.3 The Molecular "Ferric Wheel"

Systems of nanoscale or mesoscopic dimensions containing a finite number of magnetic transition-metal atoms display a number of interesting or unusual properties and have been the subject of many recent investigations [78], [79]. Properties observed include superparamagnetism [80] and quantum tunnelling [81]. Important technological applications may also be envisaged, such as magnetic refrigeration and data storage [82].

Large polynuclear organometallic molecules are among such systems, that are in the borderline of isolated and collective magnetic behavior [83], [84]. These are usually formed by a core of transition metal atoms bridged by O or S, encapsulated within a crown of organic ligands. Thus magnetic collective effects are due entirely to interactions within the molecule.

One example of such systems is the circular molecule $[Fe(OMe)_2(O_2CCH_2Cl)]_{10}$ denominated "ferric wheel" [84], of which the ground state is antiferromagnetic (S=0). A transition-metal molecule of this size constitutes a challenge for DF calculations.

Electronic structure SCF spin-polarized calculations were performed with the DV method for the cluster $[Fe(OC)_2(O_2CC)]_{10}$ formed by stripping the "ferric wheel" molecule of its peripheral H and Cl atoms (see Fig. 8) [85]. Mössbauer spectroscopy measurements have been reported [84]; calculations of the hyperfine parameters were performed and compared to experiment. The magnetic moment obtained on the Fe was $4.3\mu_B$ and the charge +2.3 [85].

The isomer shift is defined as [86]:

$$\delta = 2/3e^2\pi Z S'(Z)\Delta < r^2 > [\rho_A(0) - \rho_S(0)] \equiv \alpha\Delta\rho(0) \qquad (52)$$

where $\Delta < r^2 >$ is the variation of the mean square radius of the nucleus between excited and ground states of the Mössbauer transition, S′(Z) is a correction for relativistic effects, and the term is brackets is the difference between the electron density at the nucleus in the absorber A and source S (in other words, between a given compound and a standard system). As defined, δ is linear against $\rho(0)$ for a series of compounds or ionic states of Fe. In a non-relativistic approximation, only orbitals containing s-states of Fe contribute to $\rho(0)$.

The quadrupole splitting ΔEQ of the excited state of the 14.4 KeV transition of ^{57}Fe is given by [86]:

$$\Delta EQ = 1/2\ eV_{zz}Q\left(1+\frac{\eta^2}{3}\right)^{1/2} \tag{53}$$

where Q is the quadrupole moment of the nucleus in the excited state (I=3/2), V_{zz} the electric field gradient and η the asymmetry parameter.

The electric field gradient is produced by the non-spherical charge distribution of the nuclei and electrons around the probe nucleus. It is a traceless tensor whose components are defined as

$$V_{ij} = \frac{\partial^2 V}{\partial x_i \partial x_j}\ (x_i, x_j = x, y, z) \tag{54}$$

where V is the eletrostatic potential. Each one of the six independent components of the symmetric tensor was calculated with the expression (in atomic units) [87]-[90]:

$$V_{ij} = -\int \rho(\vec{r})(3x_ix_j - \delta_{ij}r^2)/r^5 dv + \sum_q Z_q^e(3x_{qi}x_{qj} - \delta_{ij}r_q^2)/r_q^5 \tag{55}$$

The first term in Eq. (55) is the electronic contribution, obtained with the molecular $\rho(\vec{r})$, and the second term the contribution of the surrounding nuclei shielded by the core electrons, with effective charge Z_q^e. After diagonalization, the electric field gradient is defined by the convention:

$$|V_{zz}| > |V_{yy}| \geq |V_{xx}| \tag{56}$$

with the asymmetry parameter η given by:

$$\eta = \frac{V_{xx} - V_{yy}}{V_{zz}} \tag{57}$$

The Contact (or Fermi) component H_c of the magnetic hyperfine field at the Fe nucleus may be expected to be by far the largest in the present compound. H_c is proportional to the spin density at the Fe nucleus

$$H_c = (8\pi/3)g_e\mu_B[\rho_\uparrow(0) - \rho_\downarrow(0)] \times \frac{1}{2} \tag{58}$$

In Table I are given calculated and experimental values of δ and ΔEQ. The sign of the latter was not determined experimentally. The magnetic hyperfine field was not measured, since at 4.2K no magnetic splitting of the Mössbauer lines was observed [84]. In calculating the spin-density at the Fe nucleus, only the valence contribution is obtained from the molecular calculation. The core contribution is obtained from a separate calculation for a free Fe ion with the configuration as found for the molecule. This is due to the lack of flexibility of the core basis, which inhibits spin-polarization.

3.4 Molecular Fragments

In this section we wish to show how analysis of molecular fragments, using the embedding scheme described previously, relates to properties of the complete system. In particular we focus on the convergence of the electronic charge distribution around the active center of a penta-coordinate Ru complex, whose catalytic activity is of great interest. Selective catalysts for oxidation of organic compounds generally involve the formation and stabilization of metal-oxo intermediates. Chelating ligands containing amide donors have received considerable attention [92], notably including porphyrins and macrocyclic amides which impose a rigid planar array of four donor atoms [93]. The recent discovery of a Ru^V oxidation catalyst, and analysis of the related Ru^{VI}-oxo complex has shown the possibility of utilizing a more flexible coordination geometry and properties of the d^3 metal configuration [94]. These novel electron-rich systems with flexible ligands have important implications for oxidation catalyst design and may give insight into performance of the hypothetical d^3 perferryl species.

Semiempirical molecular orbital (MO) analyses have been made to rationalize and predict the relative stability of penta-coordinate transition metal complexes [95]. Symmetry arguments and Hückel-type MO calculations on model compounds were used to discuss σ- and π-bonding interactions of D_{3h} trigonal bipyramidal (TBP) and C_{4v} square pyramidal (SP) geometries for d^n metal configurations. Discussions specific to d^2 oxo complexes have focussed upon the interrelation between planar and distorted ligand structures and amido-N σ– and π-donor capacity [96]. Properties of the newly discovered paramagnetic mono-oxo ruthenium complex $Pr_4N[Ru^V(O)PHAB]$ and the diamagnetic complex $[Ru^{VI}(O)PHAB]$, where H_4PHAB is *bis* 1,2-(2,2-diphenyl-2– hydroxyethanamido) benzene, have been similarly interpreted in terms of MO calculations on $[RuOH_4]$ complexes of TBP and SP symmetry [94]. Both complexes facilitate C-H bond activation and oxygen atom transfer reactions, and in addition the Ru^V complex catalyzes the air oxidation of triphenylphosphine.

In order to obtain a more quantitative understanding of metal-ligand interactions and the relationships between electronic structure, coordination geometry, and reactivity of the Ru penta-coordinate environment, DV calculations were undertaken on several related complexes [97], including $[RuOH_4]^q$, $[RuOCl_4]^q$ and $[Ru(O)PHAB]^q$ with q=0, -1. Anyone who has done quantum chemical molecular calculations will recognize that the terms "Ru^V, Ru^{VI}" with nominal configurations $4d^3 5s^0 5p^0$ and $4d^2 5s^0 5p^0$ represent an oversimplification of the electronic structure, which may be nevertheless very useful for qualitative discussions. The enormous Coulomb forces implied by ionic charges of +5 and +6 would immediately be screened by electron density from the ligands; it is this effect which we wish to discuss here. We choose the most extreme case, of $[Ru^{VI}(O)PHAB]^O$ for analysis, with atomic coordinates of the first coordination shell given in Table II, and analyze 6,20, and 36 atom fragments centered on Ru, along with the entire molecule. The Ru Mulliken populations and net charges on Ru and the three oxygen and two nitrogen ligands are presented in Table III. The present data are derived from *neutral* fragments, which represent an unbiased starting point; clearly the atomic charges found on the larger clusters provide information which can be used to refine the model for smaller clusters.

The fragment results, along with the entire molecule, give a consistent picture; the charge state of "Ru^{VI}" is actually something like Ru^{+2} $d^{5.7}s^{0.1}p^{0.2}$. In addition to the two d-electrons invoked in bonding interactions in semiempirical models, with low-lying empty d-states supposedly responsible for catalytic activity, we find an additional ~ 3.7 d-electrons involved in metal-ligand bonding. It is important to note that the screening mechanism which we expected is found to be short range; i.e., it derives from additional localized d-occupancy through covalent charge sharing with the ligands, and not with diffuse metal s, p charge. A typical MO near the top of the valence band is found to be a strong covalent mixture of Ru-d and ligand-p character. Analysis of corresponding "Ru^V" fragments and complexes leads to the identical conclusion, with an additional twist: the net d-populations hardly change in the two chemically distinct Ru^V and Ru^{VI} environments. This implies that understanding of the strong differences in stability and catalytic activity observed in the two species will rest more upon interpretation of modifications of the ligand p-electron structure, which is so intimately mixed with the rather stable metal d configuration.

3.5 Relativistic Effects in Molecules with 5d-metals

3.5.1 $[Ir(CN)_5]^{3-}$

The ligand CN forms bonds with transition-metal atoms that are very covalent in nature, resulting in strong electronic delocalization. Added to this, the presence of a relativistic atom induces complex and interesting effects. The low-spin complex ion $[Ir(CN)_5]^{3-}$, in which Ir is in the unusual formal oxidation state +2, has been obtained by irradiation of the hexacoordinated diamagnetic Ir(+3) complex with electrons or X-rays in solid alkali halide matrices [98]. $[Ir(CN)_5]^{3-}$ has a square-pyramidal structure (see Fig. 9) and one unpaired electron in the HOMO.

The electronic structure of $[Ir(CN)_5]^{3-}$ has been obtained with the DV method in both the non-relativistic and relativistic frameworks, to assess the relativistic effects in the chemical bonds [99]. The basis functions used for Ir were $4f_{5/2}$, $4f_{7/2}$, $5s_{1/2}$, $5p_{1/2}$, $5p_{3/2}$, $5d_{3/2}$, $5d_{5/2}$, $6s_{1/2}$, $6p_{1/2}$ and $6p_{3/2}$. All other orbitals were kept in the core. For C and N all orbitals were included in the variational space.

In Table IV are given the populations and atomic charges derived from the calculations. It is seen that the main difference in the Ir populations is in the 6s orbital, which acquires 0.14 electrons in the relativistic calculation (from 0.09 to 0.23). This is due to the stabilization of the MO's containing 6s, an effect discussed in Section 2.8, and which is also seen in the energy levels. On the other hand, 5d-containing MO's are destabilized by relativistic effects and thus the 5d population slightly decreased. The overall charge on Ir is slightly less positive in the relativistic calculation. The charges on C and N, as expected, hardly change at all.

In Table IV are also compared the bond orders for the nonrelativistic and relativistic calculations. There is a significant increase of the Ir-C bond order due to relativistic effects: therefore the latter contribute to stabilize the molecule. On the other hand, as expected, the C-N bond order is not affected.

3.5.2 Metal-cluster Halogen Complexes

As discussed in section 2.8, relativistic effects on the valence electronic structure of atoms are dominated by spin-orbit splitting of (nl) states into (nlj) subshells, and stabilization of s- and p-states relative to d- and f-states. Here we examine consequences of relativistic interactions for cubo-octahedral metal-cluster complexes of the type $[M_6X_8X_6]$ where M=Mo, Nb, W and X=halogen, which have a well defined solution chemistry, and are building blocks for many interesting crystal structures.

Relativistic effects will be largest in the tungsten complexes, and it is useful to begin with the W_6 fragment, where the nominal $W^0 5d^4 6s^2 6p^0$ configuration is expected to produce a typical metallic s-d band straddling the Fermi energy. As shown in Fig. 10, this is the result for both nonrelativistic (NR) and relativistic (R) calculations, using interatomic distances [100] taken from the chloride complex $[W_6Cl_8Cl_6]^{2-}$. Note that the nominal valence of tungsten is +2 in this complex; i.e., with configuration d^4s^0.

As we see from the figure and the populations of Table V, our expectations are fulfilled; the bare cluster reveals a normal s-d band with populations shifted from d–> s,p in the R case.

An extensive study has recently been made of $[W_6X_8X_6]^{2-}$ clusters, comparing DF theory, Hückel MO results, an experimental luminescence and absorption bands [101]. Here we focus mainly on the NR vs R consequences. The Mulliken populations and net atomic charges of the $[W_6X_8^iX_6^a]^{2-}$ clusters obtained from NR and R DV calculations are presented in Table VI. The symmetry type of the frontier orbitals and the gap between the HOMO and LUMO are summarized in Table VII; experimental absorption edge and emission maxima are also included. The atomic orbital compositions of the HOMO and LUMO from the two calculations differ primarily in their W 5d content, in the order NR> R as expected.

The presence of a bonding-antibonding (B-AB) gap or valence band-conduction band gap (VB-CB) of ~ 2.7eV is a dominant feature of the NR results. The NR and R levels correlate to each other as follows: $a_1 \longrightarrow \gamma_6$, $a_2 \longrightarrow \gamma_7$, $e \longrightarrow \gamma_8$, $t_1 \longrightarrow \gamma_6 + \gamma_7$, $t_2 \longrightarrow \gamma_7 + \gamma_8$ (for both gerade (g) and ungerade (u) representations), where γ_6, γ_7 and γ_8 are the (2-,2-, and 4-fold) irreducible representations of the double-group O_h^*. Correlations between the NR and R energy levels of the chloride are shown in Fig. 11; we see that R splitting and energy level shifts act to considerably reduce the band gap.

While the formal charges on the metal and halide atoms are +2 and −1, respectively, one would expect smaller values if covalent bonding is present within the clusters. The NR calculations produce charges which suggest a high degree of covalent bonding within the cluster, especially within the W_6X_8 core, and are similar to those calculated for the analogous molybdenum clusters [102]. It can be seen that as one goes through the halide series, the charges on the metal become significantly smaller, 1.07>0.50>0.75 for Cl, Br, and I respectively, indicating increasing covalent bonding. Absolute values of Mulliken charges of course depend upon the basis set; however, trends and shifts have great interpretative value. The net charges are consistent with experimental chemical data; i.e., the stronger covalent bonds within the cluster core (as compared with the W-

X^a bonds) predicted by the DV calculations is seen in the substitution chemistry of the cluster. The outer ligands are fairly labile and can be replaced under mild conditions, but the inner halides are much more tightly bound and only can be replaced under harsh conditions. The NR results (Table VI) give Mulliken populations for the three clusters showing a smooth trend of increasing W 5d, 6s, 6p occupancy in the halide series; there are significant contributions from the tungsten 6s and 6p orbitals. There is a small but significant halide d-orbital contribution, 0.07-0.09e in the NR case; the largest values are found on the inner Cl, indicating there a direct Cl-d participation in bonding. Table VI also reveals the considerable effects of relativity on the charge distribution; while the general trends of the NR case are preserved, the magnitude of ionic charge transfer is accentuated. The R populations show the expected shifts in orbital occupation compared with the NR results; some electron density has moved from the W 5d, X^i and X^a p orbitals into the W 6s and 6p and (to a lesser extent) X d orbitals. The net W $5d_{(3/2,5/2)}$ occupancy of $3.40 < 3.80 < 3.94$ for X=Cl, Br, and I respectively is thus considerably less than in the NR model, and also less than the formal W^{2+} d^4 value. An increase in the W $6s_{1/2}$ $6p_{(1/2,3/2)}$ occupancy across the series is noted. Both X^i and X^a d orbitals have gained significant electron density; apparently the more diffuse R orbitals are useful for bonding to the cluster core. The net R halide d-occupancy decreases from 0.51 to 0.11 for X^i and from 0.20 to 0.11 for X^a across the series. The greater contribution of the X^i d orbitals for the smaller halides apparently offers greater stabilization through directional covalent bonding.

The emission spectra of the $[W_6X_8^iX_6^a]^{2-}$ clusters are dominated by bands in the red and infrared [103]. It has been suggested that the emission maximum corresponds to the transition from the LUMO to the HOMO; Hückel MO calculations support this interpretation [102]. However, the extremely long emissive lifetimes (2.2, 16 and 26 μs for Cl, Br and I, respectively), similar to those displayed by the related molybdenum clusters, may be assumed to be the result of a *spin-* and symmetry-forbidden transition. The trend in emission energies seen in the series from chloride to iodide, with band maxima at 1.83 (Cl), 1.85 (Br) and 2.05 (I) eV, suggests that there is some halide character in the HOMO and/or LUMO, consistent with our calculations. This blue shift with increasing ligand size is, however, contrary to that expected (and calculated by DF) for the unoccupied MOs; thus the emissive state may represent a triplet, with energy significantly shifted with respect to the LUMO. Experiments with ligand substitution show that the shift in emissive energy varies more with the inner halides than the outer ligands, indicating that the inner halides give the primary ligand contribution to the frontier orbitals. Since the absorption bands are strongly blue-shifted with respect to experimental emission bands, we suppose (along with other authors) that excitations into the AB peak rapidly decay by a nonradiative process into a long-lived low lying triplet. Our previous study on the Mo_6-based analogs suggests that geometric distortion accompanies this process [102]. The present results indicate, and the observed temperature dependence of the emission bands suggests, that most likely geometric relaxation and excited-state multiplet structures must be taken into account in order to predict emission quantitatively.

First-principles DF one-electron ground state energy levels are not expected to show quantitative agreement with either experimental absorption or emission data. Often semi-quantitative comparisons can be made and trends can be discerned. In the present case, the NR HOMO-LUMO gap is too large in the cloride and bromide, while the iodide value coresponds quite well with the emission peak, probably by accident. The trend in gap energy is a red shift, expected due to the ligand-p atomic level systematics, 2.70>2.05>1.95 eV, the opposite of that observed in the emission data. The NR LUMO-HOMO transition is symmetry-forbidden in the chloride and bromide cases, but is symmetry-allowed in the iodide case. It can be seen from Table VII that the chloride an bromide clusters share the same HOMO, while the LUMO is the same for the bromide and iodide clusters. The HOMOs are fully occupied for all three clusters, giving as ground state a totally symmetric ^1A_g singlet.

Since there are many closely-spaced energy levels in the vicinity of E_F, it is clear that electronic absorption and emission bands involve more than a single discrete molecular orbital pair. A typical NR PDOS diagram of the chloride cluster, given in Fig. 12, shows the B-AB band gap centered around the Fermi energy E_F (set to zero), while in the R model (Fig. 12) E_F falls in the midst of a densely spaced set of levels near the top of the occupied valence band. The metal contribution is similar in all three clusters, with a partially-filled d-band consistent with the net 5d population close to 4.7-4.8. Interactions between the metals and the inner halides to produce the cluster core have resulted in a lowering of the X^i s and p orbitals relative to those of the outer ligands, reflecting the higher stability of the core. The W-X^i overlap can be seen at ca. -5 eV, while the W-X^a overlap is at higher energy (-1 to -2 eV). It is seen that the HOMO region is dominated by the X^a p orbitals, and the LUMO region contains primarily W 5d and X^a p character. The DV results thus support the interpretation that the absorption maxima for the $[M_6X^i_8X^a_6]^{2-}$ clusters are due to ligand-to-metal charge transfer transitions.

The DV results are therefore in qualitative agreement with experimental assignments. The most prominent feature in the region $E>E_F$ is the antibonding metallic peak, located at 3.5, 3.0 and 3.1 eV above the corresponding bonding peak for X=Cl, Br, and I respectively. The agreement with experimental absorption is semiquantitative; e.g., the VB-CB gap of 2.70 eV for the chloride can be compared with the band onset at 490 nm (2.53 eV) in polymethyl methacrylate (PMMC) films, which exhibit well defined absorption features at 400, 350, 310 and 280 nm (3.10, 3.54, 4.00, and 4.42 eV) at low temperature.

The broadening of both valence and conduction band due to spin-orbit splitting of levels, and the net upward shift and broadening of the W 5d component of the VB are largely responsible for the differences seen in comparing NR and R DOS in Fig. 12.

In looking at the frontier orbitals, the first observation to be made is the dramatic closing of the VB-CB gap in the R model. It can be seen from Fig. 11 that a number of VB levels in the NR case are raised in energy, and a number of CB levels are lowered when relativistic effects are considered. This is expected, in view of the atomic/ionic spin-orbit splittings of 0.73 and 1.31 eV for W 5d and 6p levels, respectively, and 0.51 eV for the Br 4p level. In addition, detailed level counting shows some mixing among the original NR VB and CB orbitals. Lifting of j-degeneracy has the striking effect here of pushing the HOMO down into the midst of the valence band, closing the HOMO-LUMO gap. In that sense the DOS diagram for the R case resembles that of a metal.

The implications of this result for spectroscopic predictions are considerable. The composition and symmetry of the HOMOs and LUMOs have changed considerably from the NR case, and we see that the HOMO-LUMO transition is now essentially irrelevant with respect to the IR emission spectra. In the simplified one-electron picture, we predict absorption in the extreme IR up to 0.7 eV for Cl-, 1.0 eV for Br-, and 0.2 eV for the I-ligand clusters. Dipole allowed one-electron transitions in the IR emission region are predicted to have a threshold at ~ 2.8 eV for Cl-, ~2.7 eV for Br-, and ~ 1.1. eV for I-ligand clusters. From the DOS diagrams, we can predict intense absorption into the antibonding peak located 4.1, 3.7 and 3.0 eV above E_F for X=Cl, Br and I respectively.

4 Solids

4.1 Magnetism and Superconductivity in Borocarbides

The recently synthesized rare-earth quaternary borocarbides such as RM_2B_2C (R=rare earth, M=transition metal) have stimulated much interest because of interactions between their magnetic and superconducting (SC) properties. For example, superconductivity coexists with magnestism over a limited temperature range in the Dy, Ho, Er, and Tm nickel compounds [104]. The layered crystal structure can be described schematically as (RC)-$(MB)_2$-(RC)- with square four-fold coordinated R-C sheets alternating with metal boride slabs with prominent MB_4 interlinked tetrahedral units. The M atoms form a plane with interatomic distances characteristic of a metal; e.g., R(Ni-Ni)=2.45 $\AA$ in YNi_2B_2C is slightly shorter than in the pure metal (2.50$\AA$). The nature of chemical bonding in this structure and its consequences on transport properties is not immediately apparent: despite its great structural anisotropy, band structure calculations suggest [105] rather isotropic electronic densities of states. Torque magnetometry measurements of YNi_2B_2C show high isotropy [106], while superconducting critical fields of the rare earth compounds show some angular dependence [107].

Magnetic moments on the nominally trivalent R ions provide the driving force for polarization of the conduction electrons and resulting effects on superconductivity. R-moments within a given plane are found by neutron diffraction to align ferromagnetically, with the net moment lying in, or close to, the (a-b) RC plane. Below the antiferromagnetic (AF) ordering temperature, ranging from 1.5K (Tm) to 20K (Gd) in RNi_2B_2C the net moments in alternating RC planes align opposed to each other. Over a limited temperature interval, more complex incommensurate spiral c-axis AF structures are observed [108]. The existence of regions of coexistence between AF and SC states, and the detailed mechanisms by which the magnetic coupling lowers the superconducting transition temperature T_c, suppressing SC entirely for the light rare-earth compounds, pose severe challenges for theory.

We have utilized the embedded cluster DV scheme to study the electronic structure of the $Y(Ni_{1-x}M_x)B_2C$ superconductors (M=Fe, Co, and Ru), with 71 atom variational clusters centered on the substitutional site [109] as shown in Fig. 13. Bonding within the RC plane is found to be highly ionic, while B-C and Ni-B bonding structures are analyzed as typically covalent. In addition, the strong overlap between atoms in the transition metal plane has typical metallic character. Thus the entire spectrum of chemical bonding including ionic, covalent, and metallic structures is found within this peculiar crystal structure. The Ni-B slab is found to be electron-rich, as the result of charge transfer from the RC planes.

DOS analysis shows that both Ni and B character dominate the region around E_F, as also predicted by band structures. Doping by Co, Fe, or Ru causes a broadening (lattice disorder) and weakening (dilution effect) of the Ni-dominated peak which correlates reasonably well with the experimentally observed depression of T_c. A simple rigid-band+dilution model works adequately for low doping levels, but is inadequate for

$>$ 20% impurities. The integrated transition metal PDOS or net metal d-population was found to correlate strongly with T_c, as an alternative to the frequently used $D(E_F)$ peak height. A small, but significant Y 4d, 5sp DOS component reveals hybridizaton of R valence states with C, and through the B-C bonds, interaction with the M-conduction electrons which turns out to be crucial for understanding the magnetic interactions.

Variation of electronic structure with rare earth, in the series $R(Ni_{0.99}Fe_{0.01})_2B_2C$ with R=Y, Gd, Tb, Dy, Ho, and Er was studied both by theory and by Mössbauer spectroscopy [110]. Quadrupole Splittings ΔEQ and Isomer Shifts δ were obtained for substitutional ^{57}Fe; the experimental δ measuring the local electron density showed very little variation with R, while the ΔEQ displayed a systematic shift. Low temperature measurements on the Tb compound revealed a combined quadrupole and magnetic interaction on the Fe nucleus, from which the sign, $V_{zz} < 0$, was additionally determined. The calculations are in excellent agreement with $|\Delta EQ|$ of experiment, see Fig. 14, and predict $V_{zz} < 0$ in all cases. The trend of ΔEQ vs R is traced to a lattice "pressure" effect; namely, compression within the (a-b) metal plane driven by reduction of R-ionic radii with increasing atomic number. Both the positive valence (mostly d-electron) and negative core/nuclear contributions to ΔEQ increase in magnitude with (a-b) compression; the more rapid variation of the valence term leads to the observed overall decrease in the magnitude of ΔEQ.

Self-consistent spin densities and their related magnetization and exchange fields were studied in the RNi_2B_2C compounds with R=Pr, Nd, Sm, Gd, Ho, and Tm [111]. One of the main puzzles, the coexistence of SC and AF order for the *heavy* rare earth compounds, and the total absence of SC in the light-R compounds, can now be more or less quantitatively explained. Most simply, we can think of the interaction between the R 4f-moment and the (mostly Ni) conduction electrons which participate in SC pairs as a multi-link process:

1. The R 4f polarizes and is hybridized with the R 5d.
2. The 5d mixes strongly with the C 2p, polarizing it.
3. Strong C-B covalency passes the polarization wave into the Ni-B slab.
4. Paramagnetic Ni (or transition metal substituent) picks up and amplifies the polarization.
5. Induced polarization weakens the SC pairs, mostly by exchange interaction.

The most important physical parameter across the rare earth series which affects this process is the strength of the 4f-5d interaction, which depends strongly on the mean distance between shells in the ion: $<r_{5d}>$-$<r_{4f}>$. Across the R series, both radii decrease; however, the *difference* increases almost linearly with Z, rapidly weakening the f-d interaction. Guo and Temerman have previously suggested strong f-d hybridization as the main factor in suppressing SC in $PrBa_2Cu_3O_{7-x}$, in contrast to all other isostructural $RBa_2Cu_3O_{7-x}$ compounds [112]. We find, as they did, that the f-d interaction is not simply dipolar; i.e., polarization at a distance, but strongly involves f-d hybridization as permitted by the crystalline and ligand fields. As an example, Fig. 15 shows spin-density contours on the (011) plane containing Nd, Ni, B, and C in two models: with the Nd 4f in the variational space, and in the frozen core with hybridization suppressed. Large qualitative changes and quantitative reduction in the spin density ρ_s are evident when hybridization is suppressed.

The multi-link spin transfer and polarization process is best seen in a bond-line diagram (Fig. 16). Here a zig-zag path is followed, starting at one rare earth, and following the chain R-C-B-Ni-B-C-R to the oppositely polarized R ion on an adjacent RC plane. As can be easily seen, the lighter ions Pr and Nd with smaller $<r_{5d}>$-$<r_{4f}>$ strongly polarize the lattice, including the distant Ni. On the other hand the heavy, weakly coupled, Ho and Tm induce much less polarization even though Ho has a considerably larger spin magnetic moment than Pr.

4.2 γ-Fe and γ-Fe/Al Particles in Copper

Pure bulk iron in the fcc crystal structure (γ-Fe) only exists at very high temperatures (between 1183 and 1667K). However, γ-Fe may be stabilized at low temperatures as small coherent precipitates in copper or copper-alloy matrices or as thin epitaxial films on a Cu or Cu-based alloy substrate [113], [114]. Recently the interest in γ-Fe has been revived due to the existence of multiple magnetic states revealed by band-structure calculations [115], which is believed to be related to INVAR phenomena in γ-Fe-based alloys [116].

A 62-atoms embedded cluster in cubic geometry was considered to represent γ-Fe (see Fig. 17), and spin-polarized SCF calculations were performed for both the ferromagnetic (FM) and antiferromagnetic (AFM) states, at several lattice constants. For the AFM, a layered arrangement of up and down spins (illustrated in Fig. 17) was considered.

Measurements of the magnitude of the magnetic Hyperfine Field by Mössbauer spectroscopy revealed small values at small interatomic distances and much larger values at larger distances (Fig. 18) [114]. This was ascribed to a large difference in the magnetic moment between AFM γ-Fe, more stable at small lattice constants, and FM γ-Fe, more stable at large lattice constants [115]. It is the spin-polarization induced by the Fe spin magnetic moment (mainly 3d) in the s shells that originates the hyperfine field. However, the calculations of the magnetic moments for the two states AFM and FM (Fig. 19) [117] did not show such a large difference that would justify the large experimental gap in Fig. 18. The results of calculations of the hyperfine field according to Eq. (58) of section (3.3), displayed in Fig. 20, reveal that the large difference observed experimentally in the magnitude of the hyperfine fields of AFM and FM γ-Fe originates mainly from different signs of the valence electron contribution, which is positive for AFM and negative for FM, and not from large differences in the Fe magnetic moment in the the two states. This result shows clearly that the common practice of considering the hyperfine field as proportional to the magnetic moment may be very misleading.

Since many experimental studies of γ-Fe were performed for γ-Fe particles in a Cu matrix (or Cu alloy, including Cu-Al) [113], [114], it is important to probe the electronic structure of the particle-matrix systems. Embedded-cluster methods are ideally taylored to treat small particles of a metal in a host matrix, a system that would require a very large supercell in band-structure calculations. DV calculations were performed for the 14-atom Fe particle in copper shown in Fig. 21 [118]. Spin-density contour maps were obtained to assess the polarization of the Cu matrix by the coherent magnetic γ-Fe particle. Examples are given in Figs. 22 and 23 for a Fe particle in Cu and γ-Fe in Cu with two substitutional Al. If the matrix is a Cu-Al alloy, this element is known to penetrate the Fe particle [114].

It is seen from the figures that the Cu 3d electrons present a small polarization parallel to the Fe 3d, and the (4s,4p) electrons polarize antiparallel. This is also veryfied by analyzing the Mulliken populations. The polarization of the (3s,3p) electrons of Al is always antiparallel to that of the neighbors. The presence of Al substituting for Fe was found to disrupt the AFM spin arrangement: for the AFM γ-Fe particle in copper, the presence of two Al atoms resulted in non-convergence of the SCF potential, indicative of the instability of that state. In pure AFM γ-Fe the two Al impurities caused a tendency to local ferromagnetic arrangement of the host atoms. Al substitution in FM γ-Fe causes a reduction in the 3d moment of the Fe neighbors; this same result has been reported for bcc Fe with Al impurities [119].

4.3 Annite, A Silicate Mineral

Silicates make up a large part of the earth's crust, and their physico-chemical properties have obvious importance in geochemistry and minerology. Typically structurally complex, they have been mostly studied by very approximate theories with limited predictive power, including small clusters [120]. More recently, band structure studies have begun to reveal some of the secrets of the simpler silicates [121]. In this section we briefly discuss some recent DV cluster studies on *annite*, a layered iron-bearing silicate which belongs to a class of both natural minerals and synthetic materials of interest as absorbers, carriers, and catalysts [122].

Annite has a mica-like layer structure with the monoclinic space group C2/m and two molecules per unit cell. It has the so-called 2:1 structure with a symmetric arrangement of two tetrahedral layers attached to opposite faces of a single octahedral sheet (T-O-T-K-T-O-T) [123]. The molecular formula for ideal *annite* may be written as KFe_3 $(AlSi_3)$ O_{10} $(OH)_2$ where three-fourths of the tetrahedral sites are occupied by tetravalent silicon and one-quarter by trivalent aluminum ions. Fe-atoms, nominally in the bivalent state, are octahedrally surrounded by six fourfold coordinated oxygens of two types, termed O_{TO} and O_H. Each anion is shared by three octahedra; however, each O_{TO} is also the apex of a tetrahedron whereas O_H, which is bonded to one H atom forming the OH^- group, is unshared. The hydroxyls are arranged around Fe in different positions, giving rise to *cis* and *trans* Fe^{2+} sites respectively in the ratio 2:1 along the octahedral layer. There are two other types of O, which are twofold coordinated to tetrahedral cations (Al or Si). In the present calculations they are considered to be equivalent and defined as type O_{TT}. Finally, the mobile K cations occupy the interlayer sites and ensure the electrical neutrality of the structure.

The existence of extensive Mössbauer studies of ^{57}Fe in this material provides a motivation for detailed study, since theory and experiment can be closely compared [124]. One important result of the Mössbauer work is the observation of some Fe^{3+} on the octahedral sites, presumably to relieve stress due to misfit between ionic radius of Fe^{2+} and packing requirements of the structure. Since the hyperfine fields are known to be sensitive probes of the local environment, a comparison of results with different cluster sizes and boundary conditions will give a clear indication of convergence and reliability of the model, which can be applied more generally to silicates.

Several different sites and cluster sizes were used to generate a self-consistent model of the crystal. All clusters were embedded in the potential field of the infinite ideal layered structure, with Coulomb interactions fully summed by the Ewald procedure. Two iron-centered clusters were considered to describe the O-sites: $FeO_4(OH)_2$ and $Fe(Si_4O_{14})(OH)_2$, the smaller cluster includes the first coordination shell of Fe in the variational space, and the second includes the next "shell", of silicate tetrahedra. The T-site environment was represented by variational clusters AlO_4, SiO_4 and $Al(SiFe)_3O_4$ and $Si(SiFe)_3O_4$ centered on Al and Si respectively. General features of the self-consistent atomic configurations and net charges can be seen in Table VIII; for a detailed analysis the reader is referred to Ref. [122]. The charge distributions show that the ionic character of the bonding is ordered as Al-O>Fe-O>Si-O, with self-consistent cation charge equal to +2.91, +1.90 and +3.33 for Al, Fe and Si-centered large clusters respectively. This result is consistent with the nominal electronegativities of the cation and anion. The inequivalence of three types of oxygens (O_H, O_{TO}, O_{TT}) is well described by the largest clusters, where the bonding capacity is fulfilled for O_{TO} and O_{TT}. In this case, it is observed that the charge on O tends to converge when the cluster size increases; we find the charge on O_{TT}=-1.39, -1.48 when O_{TT} is respectively bonded to Al and Si. Such a result is compatible with experiment, in which O_{TT} of two types are determined according to the occupation of the cation tetahedral site: either Al or Si. The charge on the fourfold coordinated O_{TO} converges to -1.63; it interesting to observe that this charge does not depend on the cations in $Al(SiFe)_3O_4$ and $Si(SiFe)_3O_4$ clusters. The oxygen type O_H is twofold coordinated in both Fe-centered clusters. It is reasonable to assume the configuration $2s^{1.95}2p^{5.84}$ due to the largest cluster as the most probable; however, it is worth mentioning that O_H can occupy trans and cis positions in the octahedral layer and in the present calculations the cis position is completely neglected.

With the Coulomb potentials of the crystal now determined, we may consider its magnetic properties, starting with a description of the spin-polarized valence band region. The higher-energy valence bands straddling the Fermi level are primarily of Fe 3d character, with a large exchange splitting of ~2.7 eV between spin up and spin down components. The majority spin band is fully occupied, as expected. The twofold substructure is comparable to the splitting of electronic energy levels of a high-spin d^6 ion embedded in a distorted octahedral crystal-field. Distortion of the octahedron lifts degeneracy of e_g and t_{2g} orbitals; in the relevant C_{2h} group there are no degenerate orbitals. However, the 3d states are clearly split into two distributions which are remnants of the cubic character with an energy separation between them, corresponding to the $10D_q$ parameter of ligand field theory, of ~0.6 eV. The five spin up ($\uparrow$) electrons in the filled subband are ordered in energy values as $3d_{z^2} < 3d_{x^2-y^2} < 3d_{xy} < 3d_{yz} < 3d_{xz}$. This result is compatible with the neighboring anions geometry; for example the lobes of the $3d_{xz}$ function point toward the O_H ligands. The minority spin distribution encloses the last occupied $20a_g \downarrow$ orbital with 95% Fe $3d_{z^2}$ character. The nearby conduction-band unoccupied levels are predominantly Fe 3d$\downarrow$ and Si 3s3p, with Al excited states falling to higher energy. This picture is consistent with general features of magnetic transition metal oxides; details of level composition will be revealed upon consideration of the hyperfine fields, and in particular, the Mössbauer quadrupolar splitting and the magnetic dipolar field.

The calculated spin magnetic moment on Fe is $+3.96\mu_B$, almost entirely due to the 3d-moment; this value is very close to the maximal spin of $+4\mu_B$ and compatible with the Fe^{2+} configuration. This value is in good agreement with that adopted to model the natural single-crystal *annite* in order to explain the experimental saturation magnetization derived from high-spin SQUID magnetometry [125]. The oxygen atoms gain a spin polarization moment; it is larger for the six oxygen nearest neighbors as expected: +0.014 and $+0.008\mu_B$ for O_H and O_{TO} respectively. Details of the contact spin density, electric field gradient (EFG), asymmetry parameter (defined in Section 3.3), and magnetic dipolar field (MDF) are given in Table IX. The components of the magnetic dipolar field tensor are given by:

$$M_{ij} = \mu_B \int \rho_s(\vec{r})(3x_i x_j - \delta_{ij} r^2)/r^5 dv \tag{59}$$

where μ_B is the Bohr magneton and ρ_s is the spin density $[\rho_\uparrow(\vec{r}) - \rho_\downarrow(\vec{r})]$. We find that the anisotropic EFG and MDF, which depend very sensitively upon the angular character and weight of occupied Fe 3d orbitals, differ greatly from the minimal cluster model, to the cluster with two coordination shells of neighbors. This is consistent with experience with other supposedly ionic systems, and gives some measure of the influence of covalent interactions in silicates along with other simpler oxides. The data from the larger cluster can be fit very well to the experimental Mössbauer spectra, and indicate that the EFG principal axis and the internal magnetic field H_F are parallel. This prediction can be checked in principal by making measurements at low temperature in an external magnetic field. On the strength of these results, we believe we have obtained an adequate model for the *annite* system and have established a good basis for further studies on these fascinating materials.

4.4 An Electroceramic Grain Boundary

Electroceramics include a wide variety of technically important materials with nonlinear electrical properties, including devices such as varistors, thermistors, boundary layer capacitors, and ferroelectric memories. Their behavior is largely governed by electrically active grain boudaries (GB), whose dielectric permittivity, capacitance, and resistive behavior are closely linked with microscopic geometry, chemical environment, and electronic structure. Tailoring of GB to specific needs by controlling processing conditions and incorporation of impurities forms a large part of the art of producing useful materials.

$SrTiO_3$ is one such functional electroceramic, much studied because of its relatively simple perovskite structure and its GB capacitative behavior, obtained upon aliovalent doping. Studies of GB structure by high resolution spatially resolved electron microscopy and energy loss spectroscopy have revealed enough of the local geometry, on a 3-5$\mathring{A}$ length scale, to make detailed modelling feasible [126]. Atomistic modelling has been done, using a lattice statics approach to find low energy configurations compatible with experimental data. Not only are the resulting structures complex, with different stoichiometry than the ideal bulk, but they are numerous. For example, for the well characterized 36.8^0 symmetric tilt $\sum = 5$ GB a total of fourteen low energy structures were found compatible with experiment [127]. One of these, shown in Fig. 24, was selected for detailed electronic structure studies on the basis of chemical intuition and "feel"; details are given in the literature [128], here we touch briefly on differences in Ti environment in the GB versus the bulk, and on the effects of transition metal substituents at the Ti site.

In the ideal cubic perovskite structure, Ti^{4+} is surrounded by six O^{2-} in the first coordination shell, followed by eight Sr^{2+}. DV calculations on clusters with up to ~ 50 atoms reveal a self-consistent atomic configuration of $Ti^{+2.88}\ 3d^{0.99}4s^{0.02}4p^{0.08}$ showing the considerable effects of Ti 3d – O 2p covalency. Examination of geometry around titanium in the GB core shows that most often, the local oxygen coordination is reduced from six to five; in addition, the average Ti-O bond length is significantly reduced. Self-consistent calculations show that the response of Ti at the GB core is partial reduction, with a typical configuration of $Ti^{+2.68}3d^{1.17}4s^{0.03}4p^{0.12}$ representing an accumulation of electronic charge at the GB core, relative to bulk. The strontium coordination is also reduced (from 12 to $\sim$9) in the GB, and its response is similar. In bulk, its configuration is found to be highly ionic: $Sr^{+1.93}4d^{0.04}5s^{0.01}5p^{0.03}$, while in a typical GB environment we find $Sr^{+1.66}4d^{0.31}5s^{0.03}5p^{0.03}$, reflecting accumulation of some covalent character due to reduced Sr-O bond lengths. Again, the net result is accumulation of electronic charge at the GB core, helping to build up the Schottky barrier responsible for capacitive behavior.

Deliberate doping of strontium titanate by transition metal acceptors, including Mn, Fe, and Ni which concentrate at the grain boudaries, is known to enhance the GB capacitative effect and is an essential component for commercial materials. Calculations on transition metal-doped $SrTiO_3$ were made, substituting for Ti both in bulk crystal and at the GB. A typical result for Mn shows an ideal crystal ionic configuration of $Mn^{+2.08}3d^{4.84}4s^{0.02}4p^{0.04}$; thus Mn is indeed divalent, but accepts only ~0.80e instead of the nominal 2e expected from formal valency, due to the lesser charge initially on Ti. Attempts to stabilize Mn^{3+}, which is experimentally observed at lower concentration, always led to the divalent self-consistent state. This suggests that the trivalent ion is associated with oxygen vacancies, known to exist in significant numbers, and to contribute to space charge and conduction processes. Similar calculations of Mn substitution at the GB core yield a typical configuration $Mn^{+1.84}3d^{4.96}4s^{0.07}4p^{0.11}$, showing again partial reduction with respect to the bulk state. The most significant feature here is that Mn accepts $\sim 0.84e$ at the GB core, slightly greater than in bulk, again contributing to formation of the Schottky barrier. Doping by electron donors which may concentrate in the bulk, is expected to compensate the bulk acceptors, leaving the desired space charge region around the GB.

Further studies are underway, using the MD/MC methodology described in section 2.9, to refine the local geometry in view of first-principles determination of ionic charges different from nominal values, and taking into account differing ionic radii of substituents. We see that very simple ideas arising from calculated electronic charge distribution are already useful in helping to construct viable models of electroceramic grain boundaries. More detailed theoretical analyses, relating to the X-ray near-edge abosorption and high resolution electron energy loss data, can be expected to contribute further to understanding local geometry and atomic configuration of substituents.

Acknowledgments

Part of the calculations reported were performed at the Cray Y-MP of the Supercomputing Center of the Universidade Federal do Rio Grande do Sul. Work supported in part by CNPq (Brasil) and by the MRSEC program of the National Science Foundation (DMR-9632472) at the Materials Research Center of Northwestern University, and through NSF Grant No. INT-9600016.

Figure Captions

Fig. 1 – (Insert where placed in text).

Fig. 2 – (Insert where placed in text).

Fig. 3 – Some typical porphyrinic molecules: a) Ni star-porphyrazine, with four fused thiolene groups (4PZ), b) basic porphyrazine structure with peripherally fused-benzo rings (PC) and c) dithiolene groups (PZ).

Fig. 4 – PDOS of 4PZ nickel porphyrazine, after Ref. [72].

Fig. 5 – Theoretical and experimental absorption bands of 4PZ Ni(TAP).

Fig. 6 – Views of $[Cp(CO)_2Fe(\eta^1\text{-}T)]^+$. a) $\theta = 120^0$, b) $\theta = 180^0$.

Fig. 7 – Variation of the calculated total energy of $[Cp(CO)_2Fe(\eta^1\text{-}T)]^+$ as a function of θ. a) Without 3d orbitals in the S basis, b) with 3d orbitals on the S. The reference energy is for the coplanar geometry ($\theta = 180^0$).

Fig. 8 – Views of the cluster $[Fe(OC)_2(O_2CC)]_{10}$, representing the molecule "ferric wheel". a) Top view (z=0 plane), b) Side view.

Fig. 9 – The square-pyramidal complex $[Ir(CN)_5]^{3-}$. Ir is at the center; neighbour atoms are C.

Fig. 10 – Partial and total densities of states of neutral W_6 clusters.

Fig. 11 – Nonrelativistic and relativistic energy levels of $[W_6Cl^i_8Cl^a_6]^{2-}$.

Fig. 12 – Partial and total densities of states of $[W_6Cl^i_8Cl^a_6]^{2-}$ in the nonrelativistic (top) and relativistic (bottom) models.

Fig. 13 – $R_{12}M_{15}B_{32}C_{12}$ transition-metal centered cluster representing RM_2B_2C compounds.

Fig. 14 – Experimental and calculated absolute values of ^{57}Fe quadrupolar splitting in $R(Ni_{0.99}Fe_{0.01})_2B_2C$ versus ratio of lattice parameters c/a. From Ref. [110].

Fig. 15 – Spin-density $[\rho_\uparrow(\vec{r}) - \rho_\downarrow(\vec{r})]$ contours on the (011) plane of $NdNi_2B_2C$. a) Nd 4f in variational space, b) Nd 4f placed in frozen core. Contour levels are from -0.002 to +0.002 e/au^3 with intervals of 0.0001. Full lines are positive values. After Ref. [111].

Fig. 16 – Bond-line plots of the polarization field H for antiferromagnetic RNi_2B_2C, beginning at one rare-earth and passing from atom to atom along bond lines, terminating at a R in the next plane (distance c/2) above or below. $H=(8\pi/3)\mu_B[\rho_\uparrow(\vec{r})-\rho_\downarrow(\vec{r})]$. From ref. [111].

Fig. 17 – 62-atoms cluster representing fcc Fe. Light and dark spheres represent alternating layers of spins in the AFM configuration.

Fig. 18 – Experimental values of the magnitude of the hyperfine field of fcc Fe at several lattice constants (from ref. [114]).

Fig. 19 – Calculated spin magnetic moments μ plotted against the Wigner-Seitz radius r_s of γ-Fe (from ref. [117]).

Fig. 20 – Total hyperfine field H_F and components plotted against the Wigner-Seitz radius r_s of γ-Fe (from ref. [117]). Valence electrons contribution, ·······; core electrons contribution, — — — —, total, ______.

Fig. 21 – Cluster representing a cubic particle of Fe with 14 atoms in the fcc structure, surrounded by Cu atoms. Darker spheres represent Fe.

Fig. 22 – Spin density contours for FM γ-Fe particle surrounded by copper, in the (x,z) plane. From -0.01 to +0.01 e/a.u.^{3} with intervals of 0.001 e/a.u.^{3}. Full lines are positive values. From ref. [118].

Fig. 23 – Spin density contours for FM γ-Fe particle surrounded by Cu in the (x,z) plane with two Al on the z axis substituting for Fe. Contour specifications as in Fig. 22. From ref. [118].

Fig. 24 – Schematic of 36.8^0 symmetric tilt $\sum = 5$ grain boundary in $SrTiO_3$, showing a Ti-centered variational cluster at the GB core. Small spheres: Ti, medium spheres: Sr, and large spheres: O.

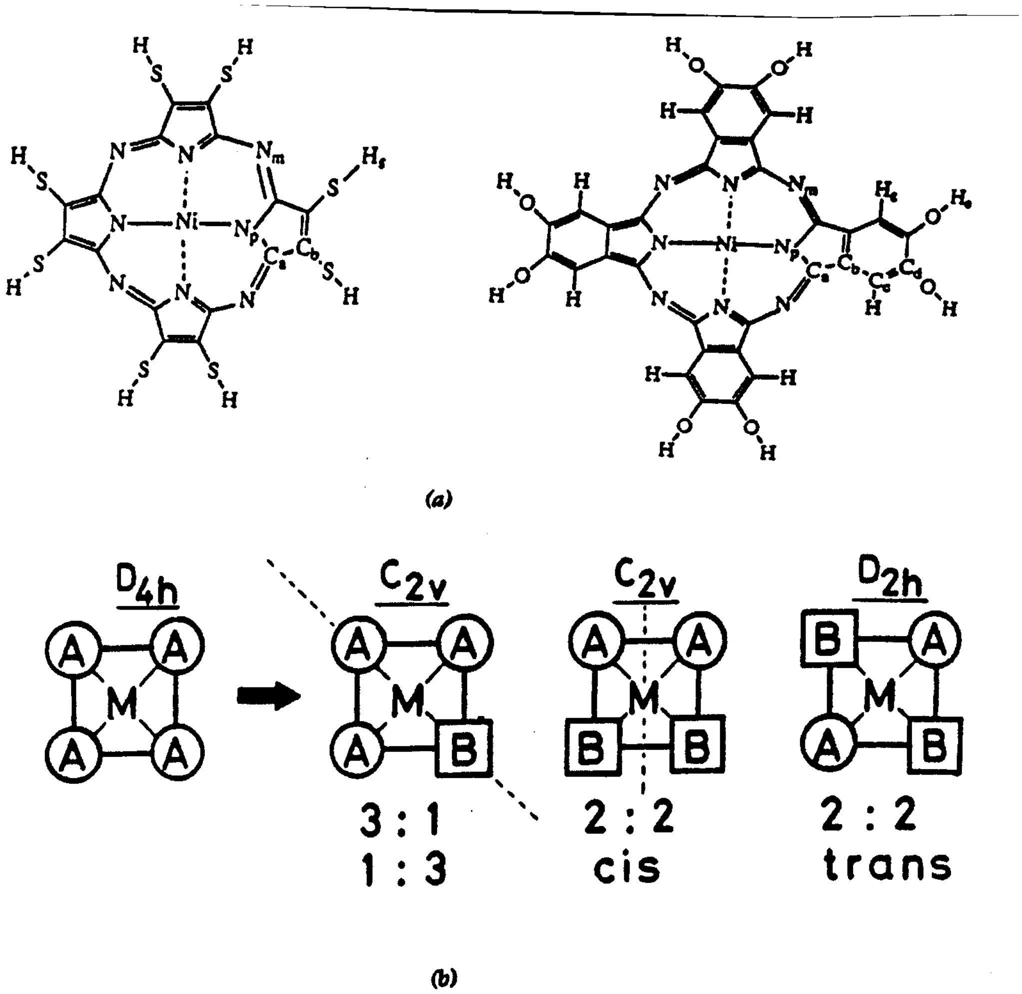

Ni
N
Nm
Np
Ca
Cb
Cc
Cd
S
O
H
Hs
He
D4h
C2v
C2v
D2h
A
B
M
3 : 1
1 : 3
2 : 2
cis
2 : 2
trans

(a)

(b)

Fig. 3

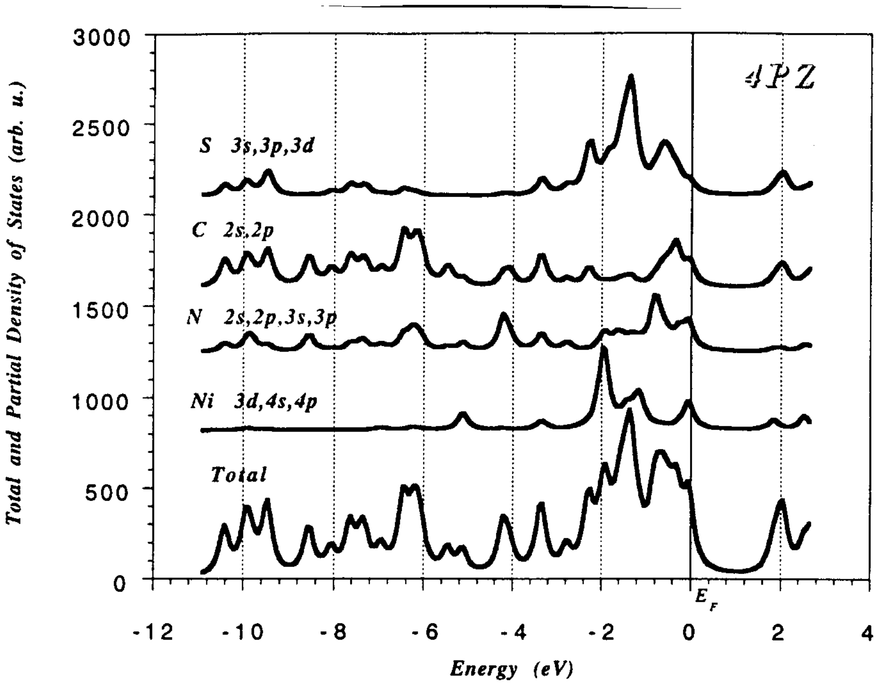
4PZ
S 3s,3p,3d
C 2s,2p
N 2s,2p,3s,3p
Ni 3d,4s,4p
Total
Total and Partial Density of States (arb. u.)
3000
2500
2000
1500
1000
500
0
E_F
-12
-10
-8
-6
-4
-2
0
2
4
Energy (eV)

Fig. 4

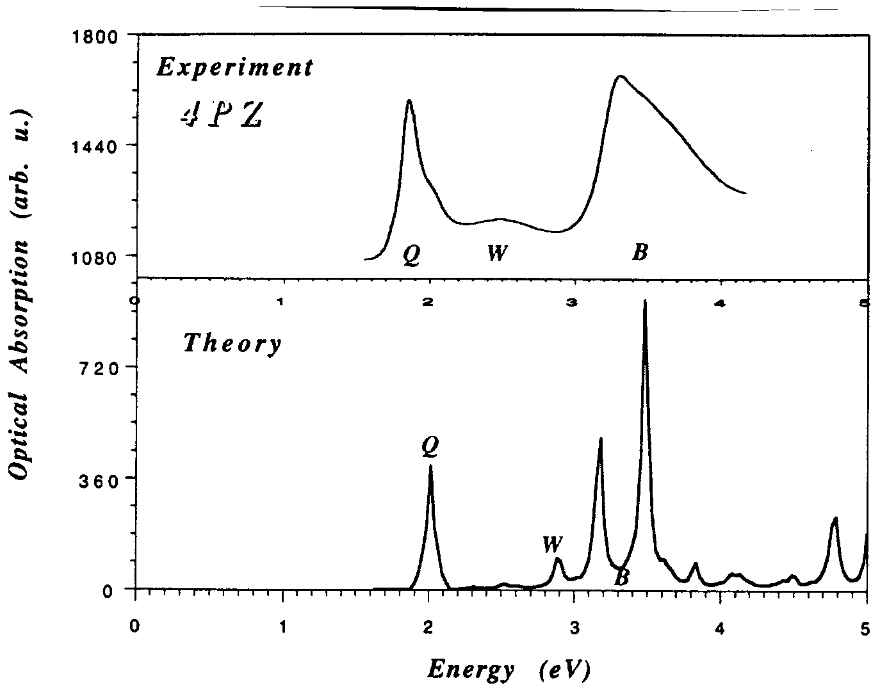
Experiment
4PZ
Q
W
B
Theory
Q
W
B
1800
1440
1080
720
360
0
0
1
2
3
4
5
Optical Absorption (arb. u.)
Energy (eV)

Fig. 5

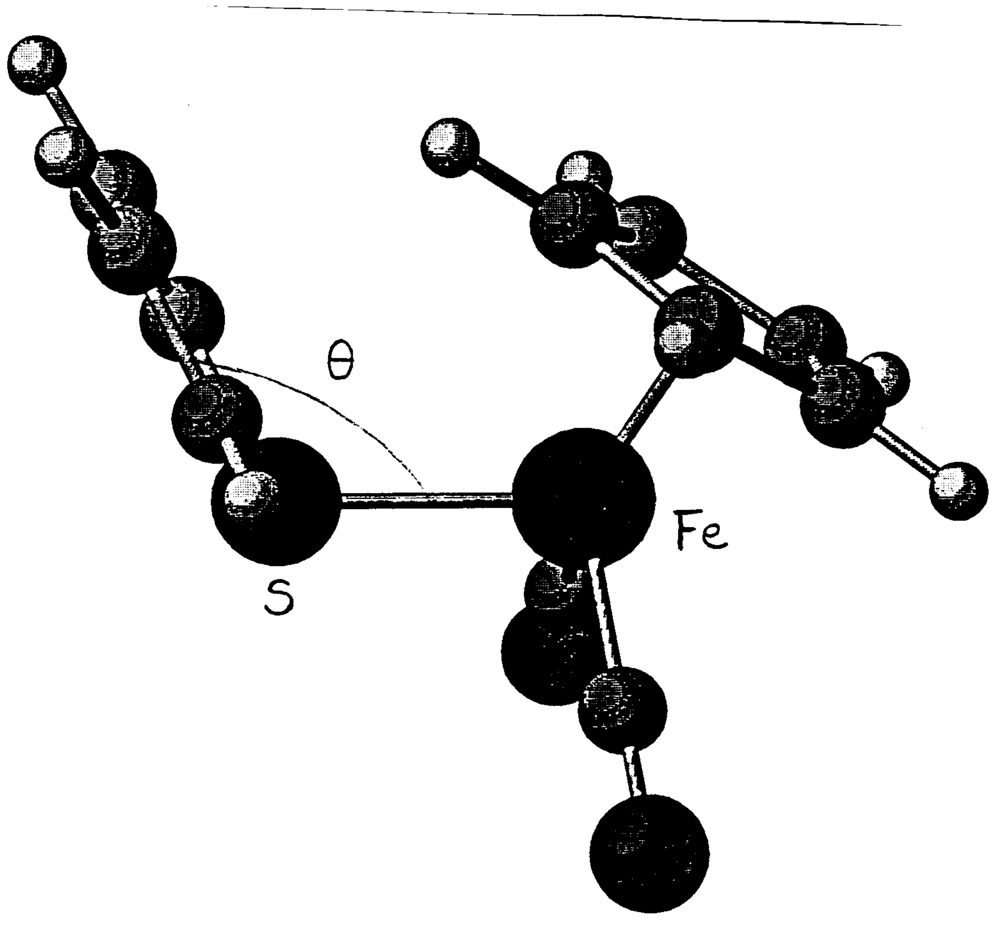

Fig. 6a

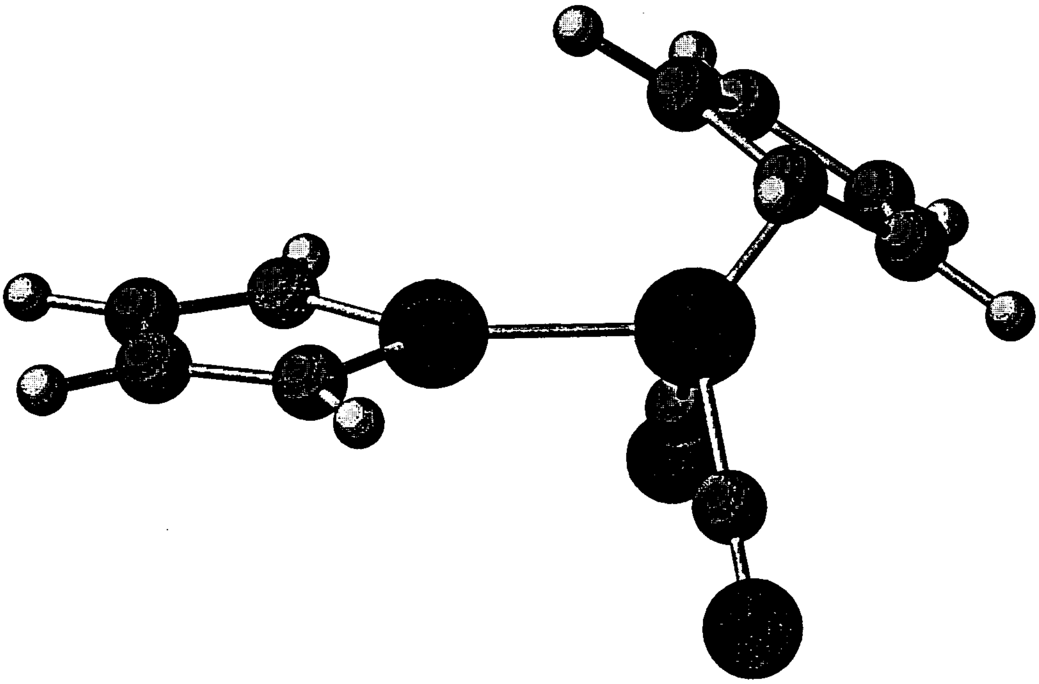

Fig. 6b

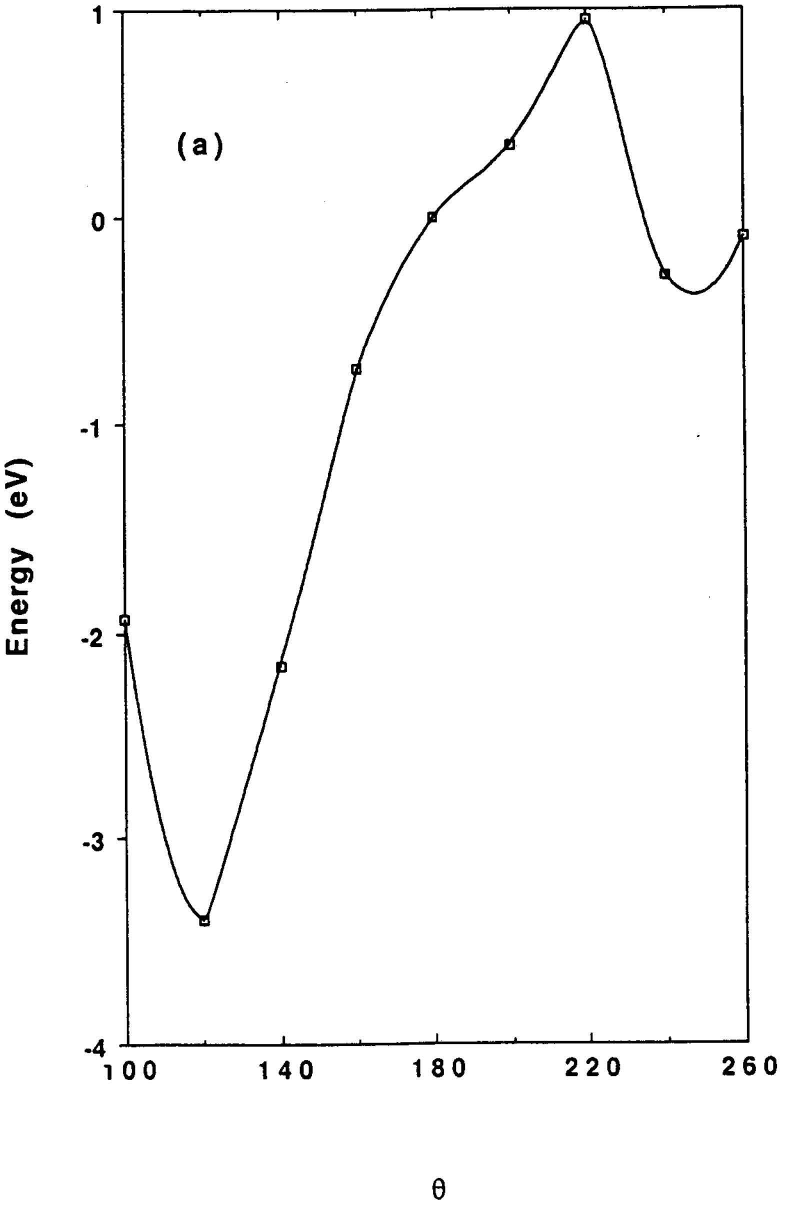

Fig. 7a

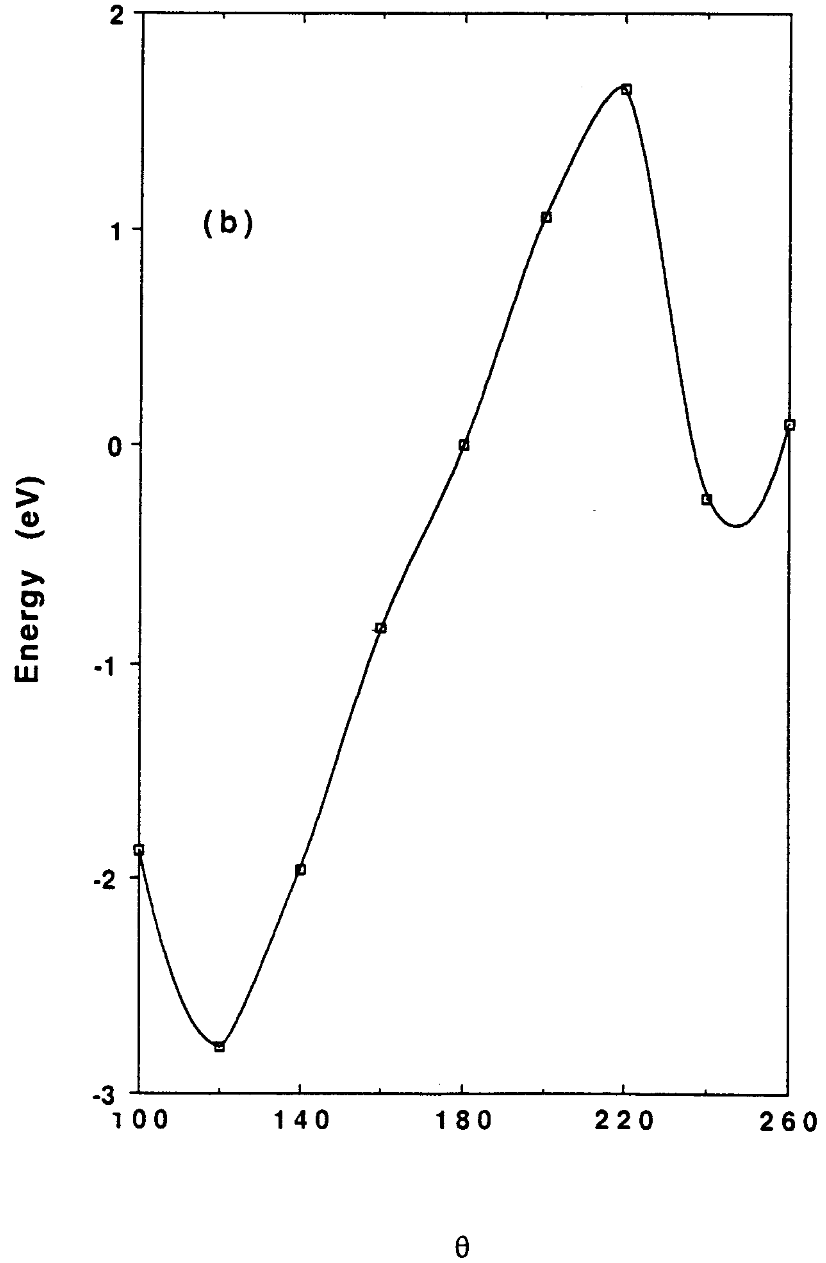

Fig. 7b

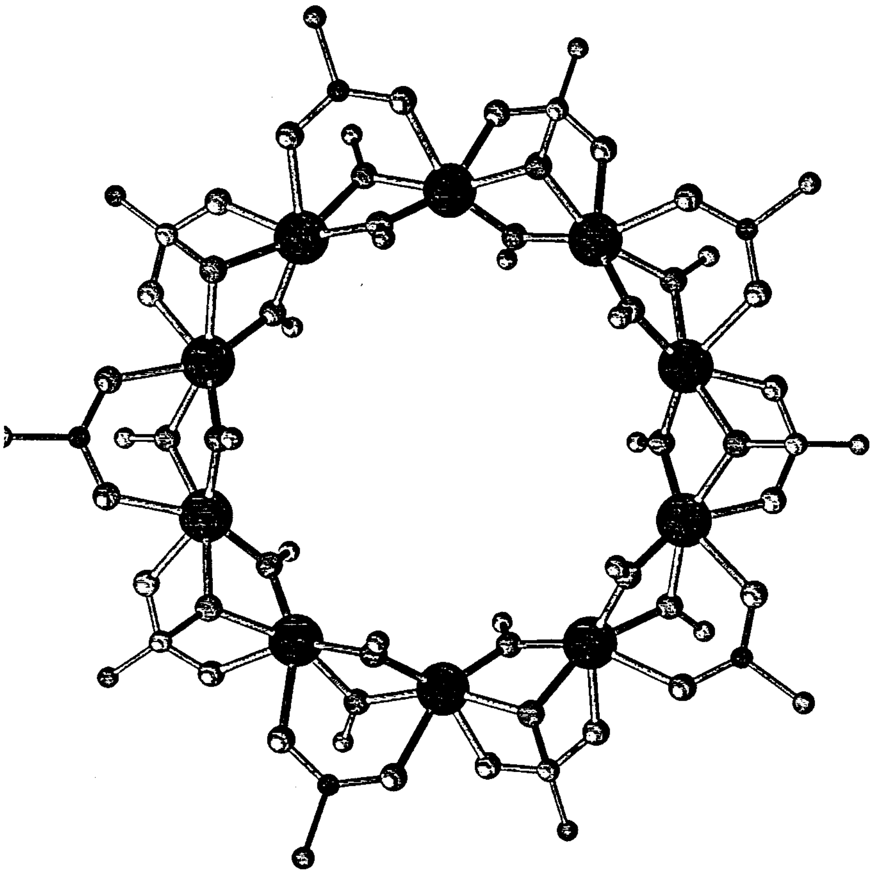

Fig. 8a

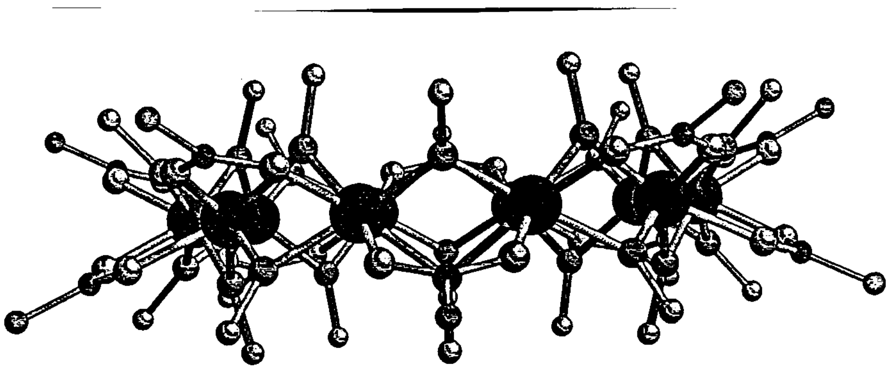

Fig. 8b

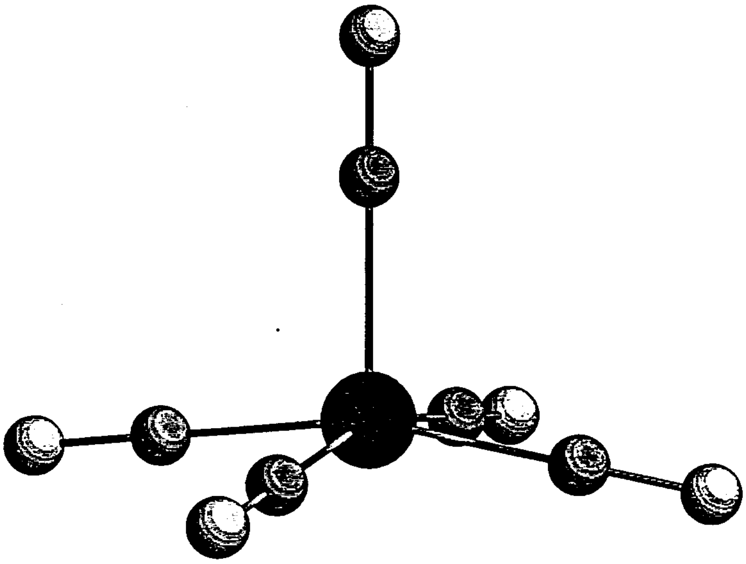

Fig. 9

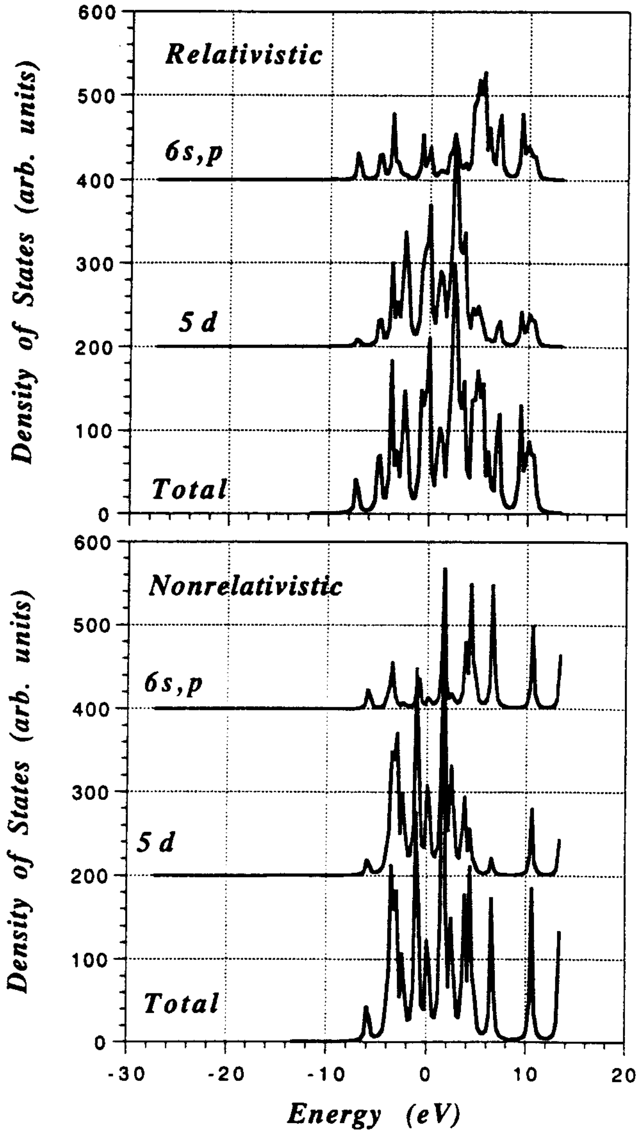
Relativistic
6s,p
5 d
Total
Nonrelativistic
6s,p
5 d
Total
Density of States (arb. units)
Density of States (arb. units)
0
100
200
300
400
500
600
-30
-20
-10
0
10
20
Energy (eV)

Fig. 10

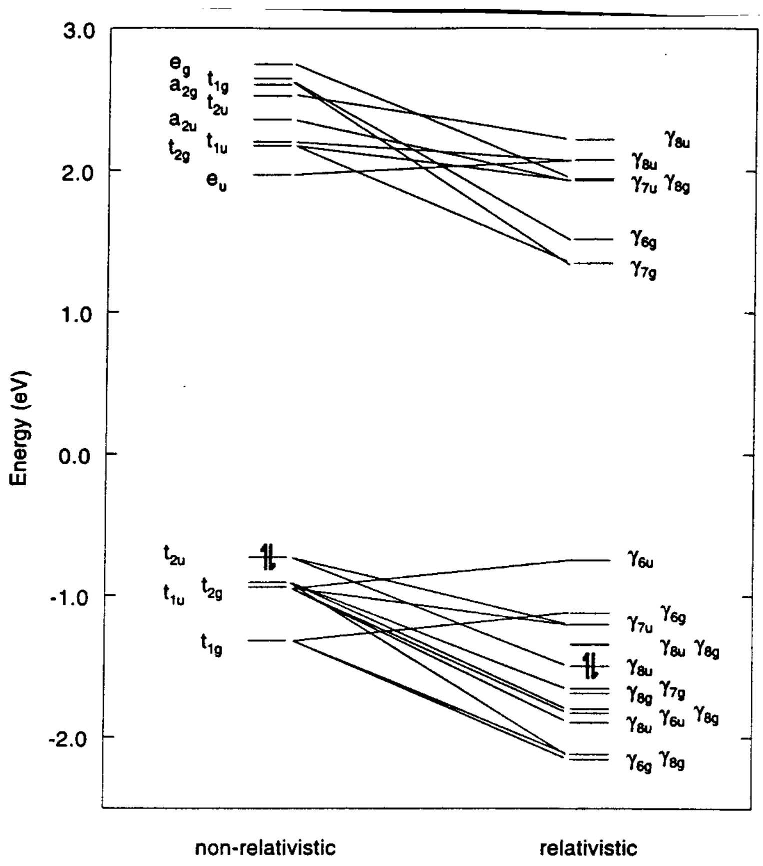
Energy (eV)
3.0
2.0
1.0
0.0
-1.0
-2.0
e_g
a_{2g}
t_{1g}
t_{2u}
a_{2u}
t_{1u}
t_{2g}
e_u
γ_{8u}
γ_{8u}
γ_{7u} γ_{8g}
γ_{6g}
γ_{7g}
t_{2u}
t_{1u}
t_{2g}
t_{1g}
γ_{6u}
γ_{7u} γ_{6g}
γ_{8u} γ_{8g}
γ_{8u}
γ_{8g} γ_{7g}
γ_{8u} γ_{6u} γ_{8g}
γ_{6g} γ_{8g}
non-relativistic
relativistic

Fig. 11

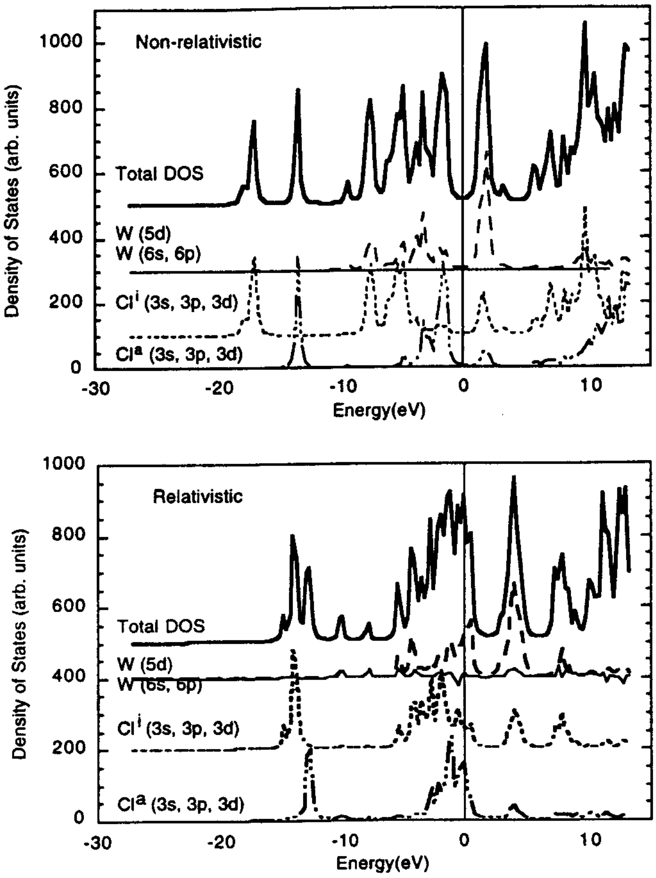
Non-relativistic
Density of States (arb. units)
1000
800
600
400
200
0
Total DOS
W (5d)
W (6s, 6p)
Cl^i (3s, 3p, 3d)
Cl^a (3s, 3p, 3d)
-30
-20
-10
0
10
Energy(eV)
Relativistic
Density of States (arb. units)
1000
800
600
400
200
0
Total DOS
W (5d)
W (6s, 6p)
Cl^i (3s, 3p, 3d)
Cl^a (3s, 3p, 3d)
-30
-20
-10
0
10
Energy(eV)

Fig. 12

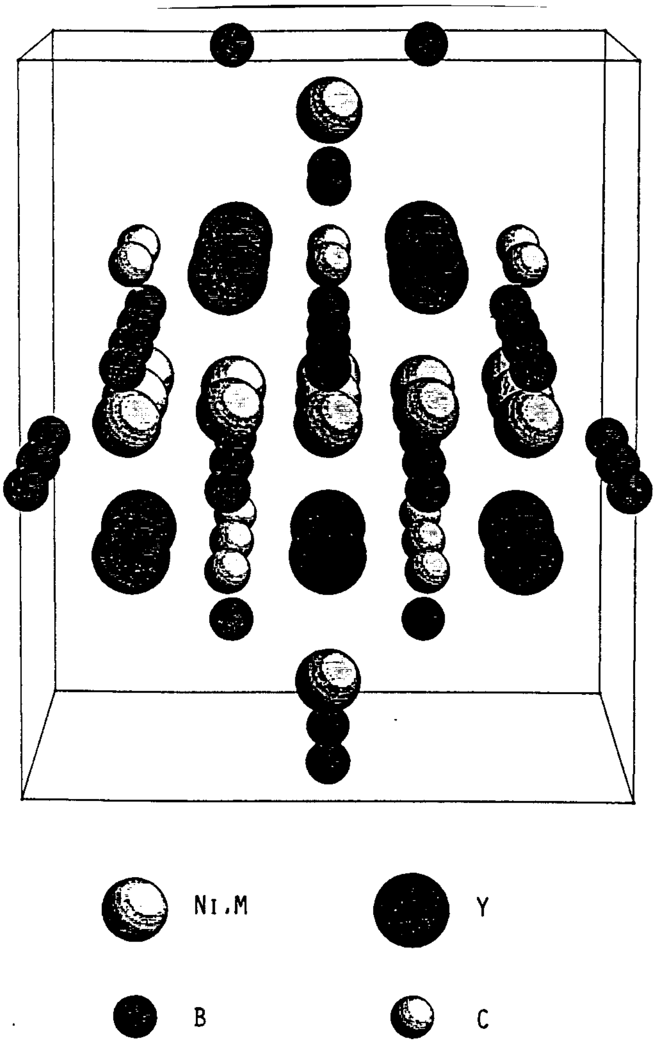

Fig. 13

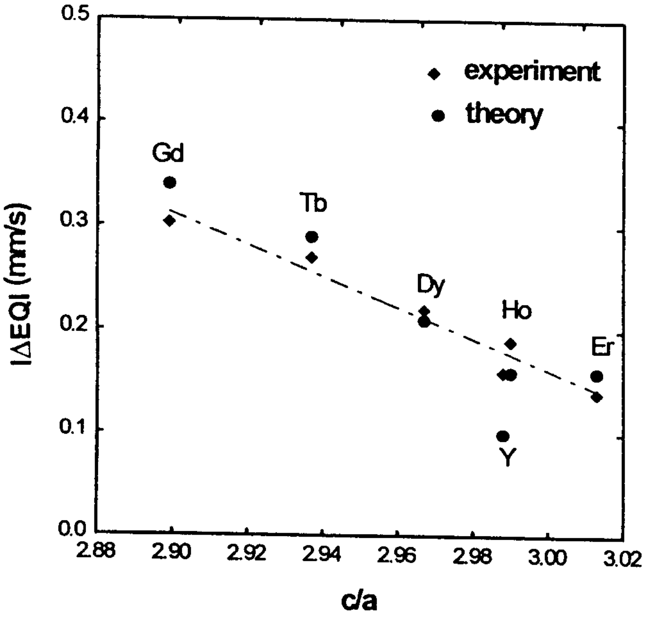
◆ experiment
● theory
Gd
Tb
Dy
Ho
Er
Y
0.0
0.1
0.2
0.3
0.4
0.5
I∆EQI (mm/s)
2.88
2.90
2.92
2.94
2.96
2.98
3.00
3.02
c/a

Fig. 14

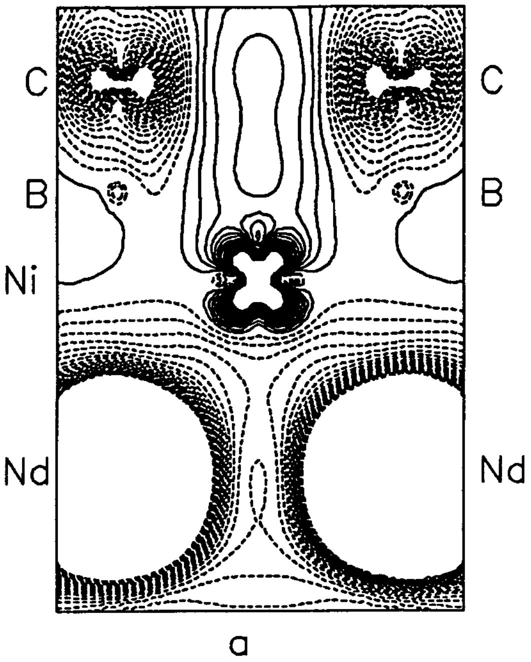

Fig. 15a

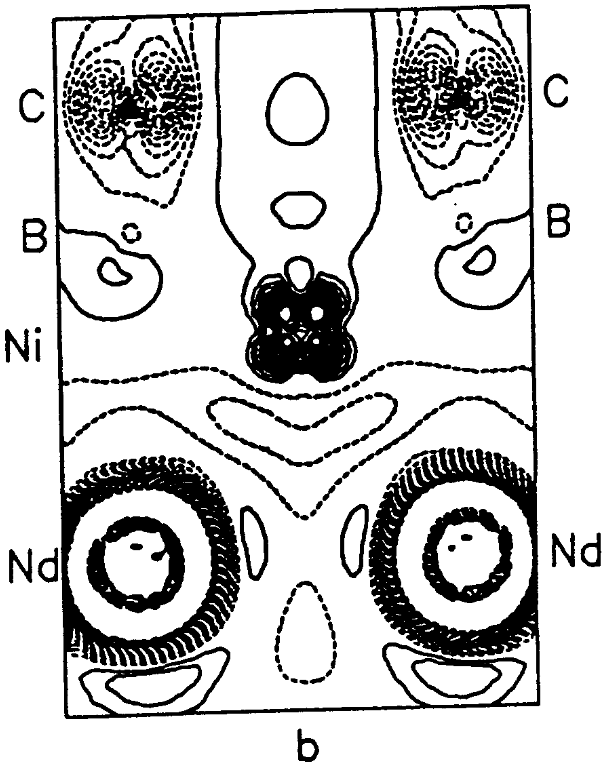

Fig. 15b

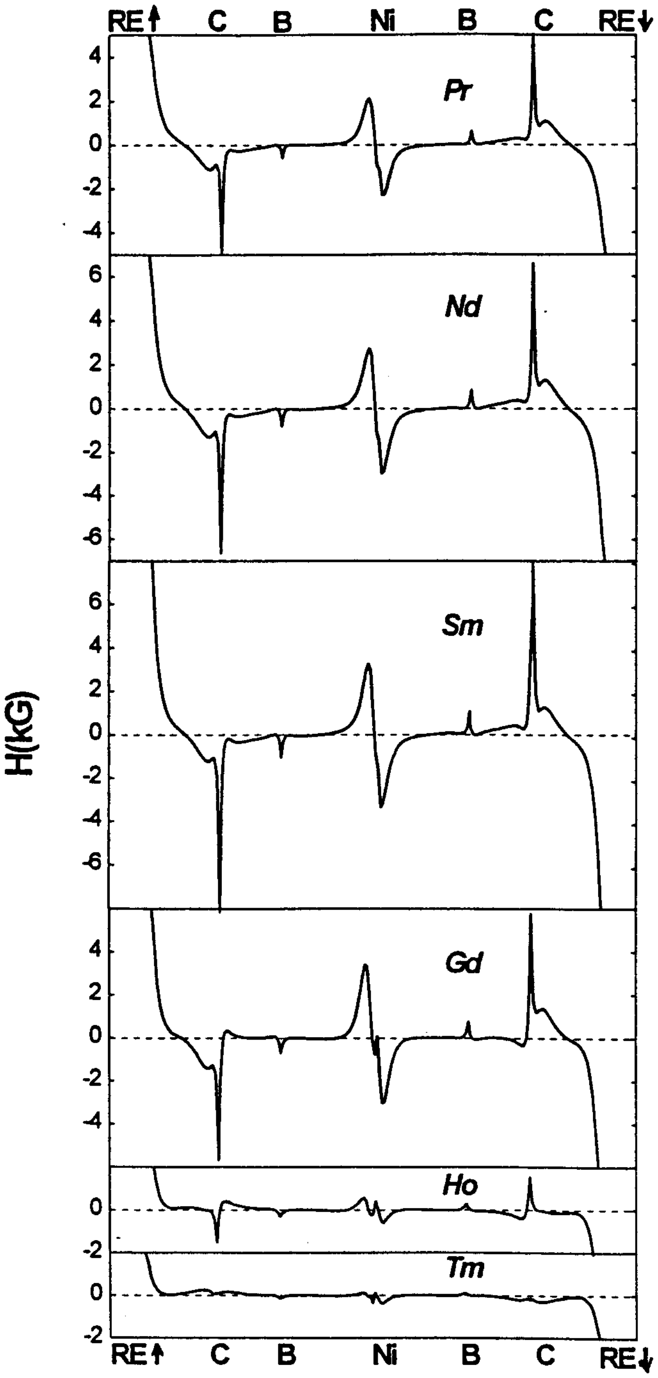

Fig. 16

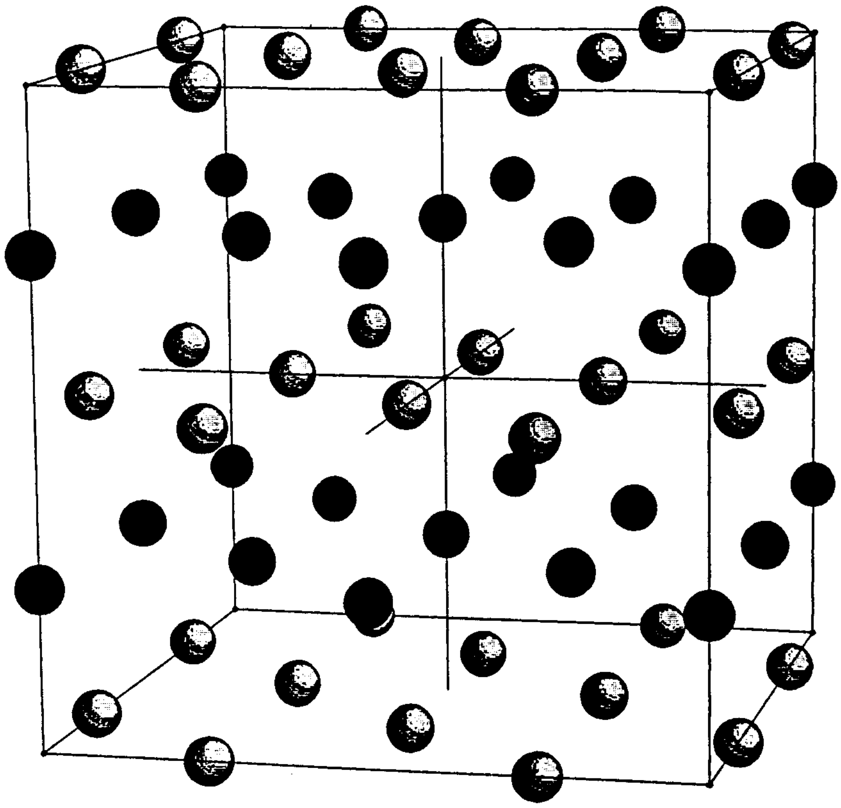

Fig. 17

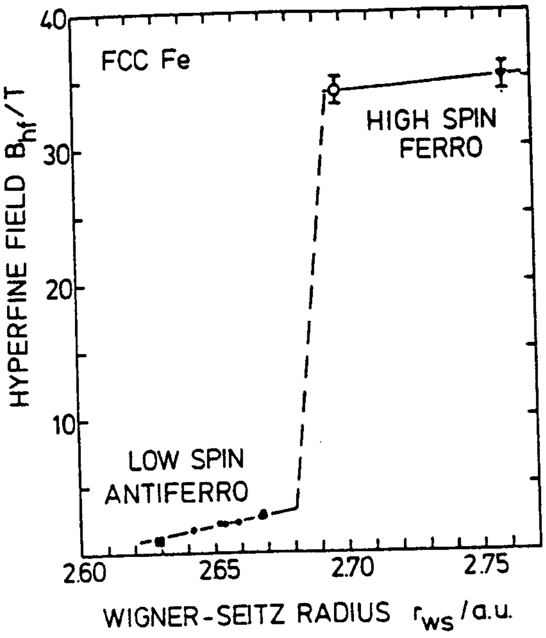
FCC Fe
HIGH SPIN
FERRO
LOW SPIN
ANTIFERRO
HYPERFINE FIELD B_{hf}/T
40
30
20
10
2.60
2.65
2.70
2.75
WIGNER-SEITZ RADIUS r_{WS}/a.u.

Fig. 18

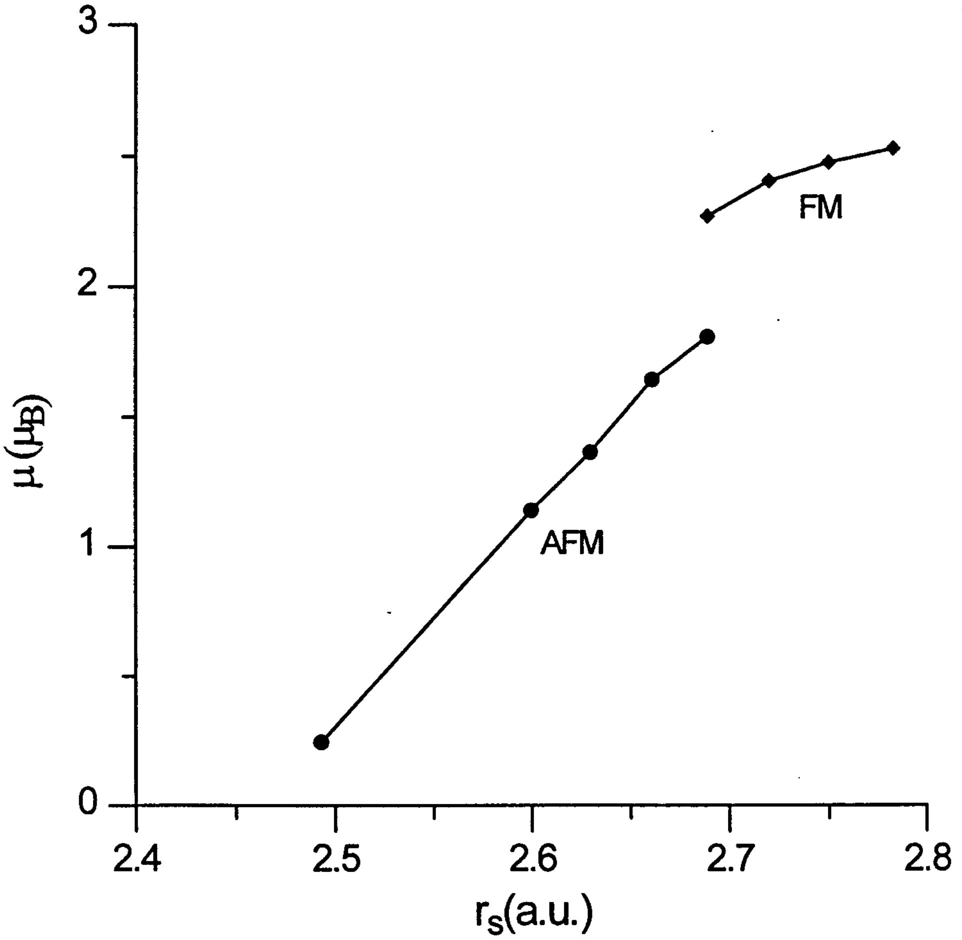

Fig. 19

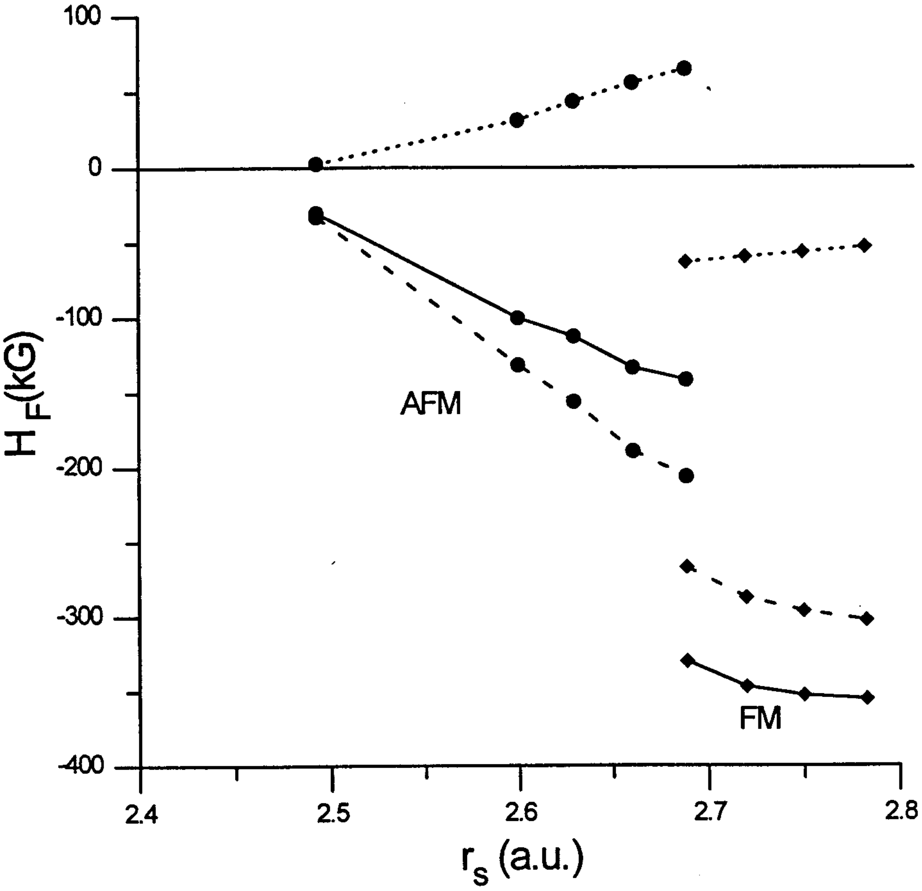

Fig. 20

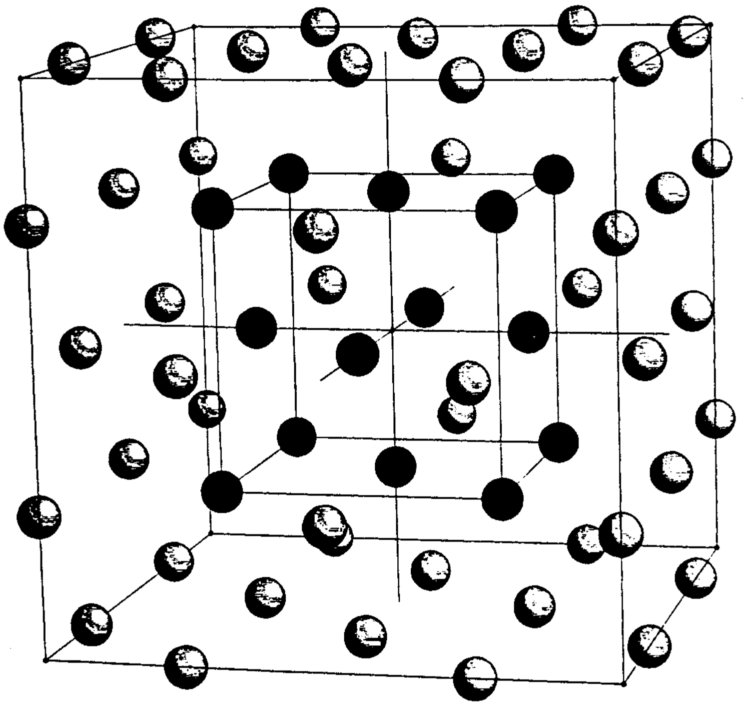

Fig. 21

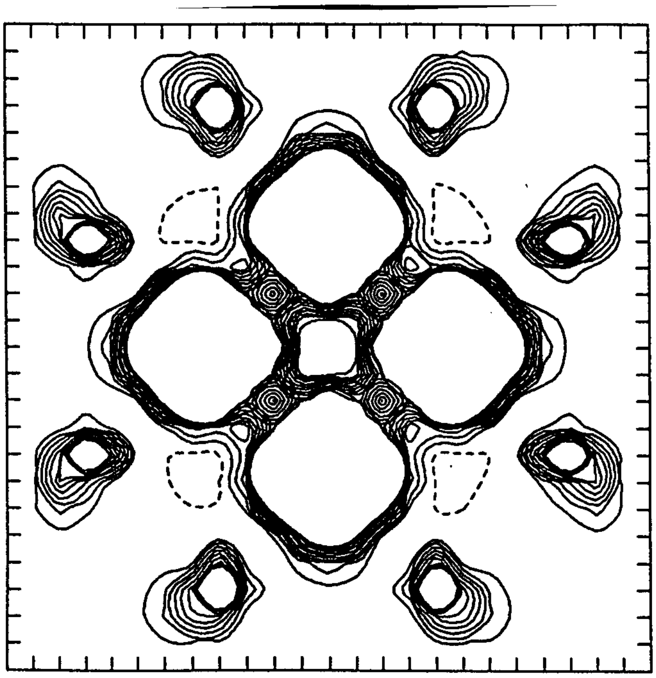

Fig. 22

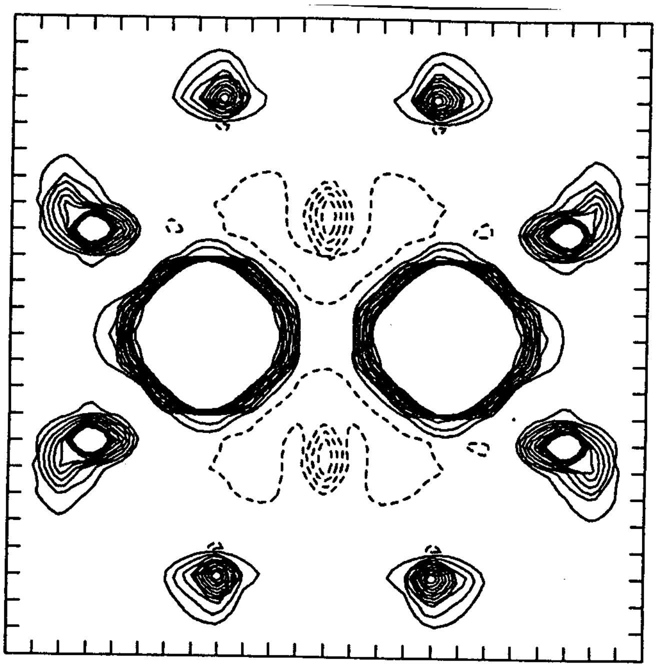

Fig. 23

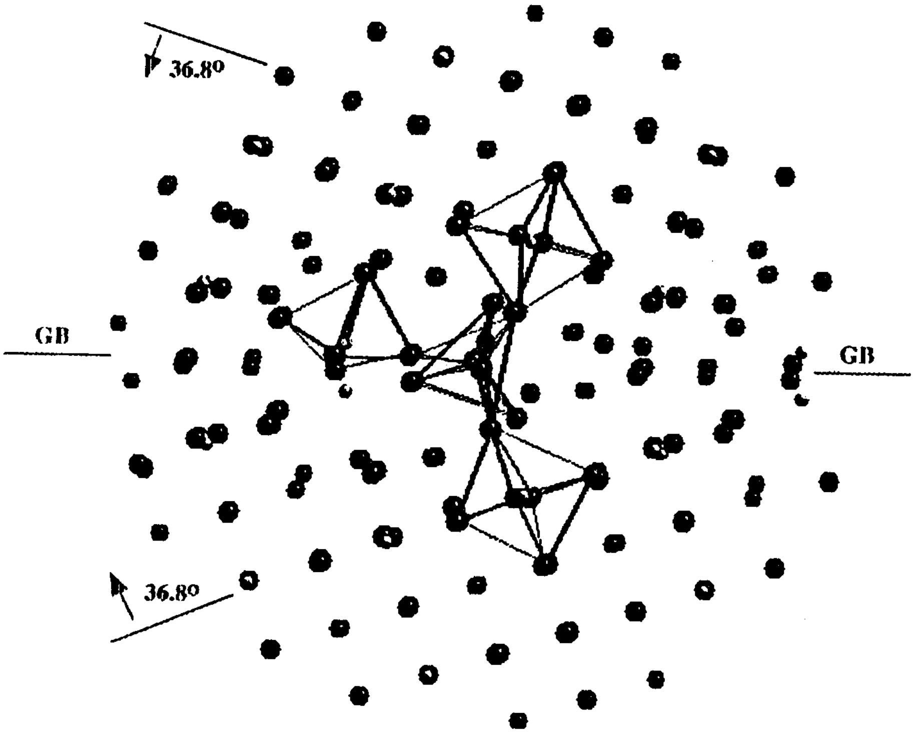

Fig. 24

Table I – ^{57}Fe hyperfine parameters of $[Fe(OMe)_2(O_2CCH_2Cl)]_{10}$. Values of the isomer shift δ relative to Fe metal. Value of α from ref. [87].

Isomer Shift

$\rho(0)(a_0^{-3})$ (3s+valence)	$\delta(mm/s)$ (calculated)	$\delta(mm/s)$ (experimental)^a
145.43	0.48	0.52

Electric field gradient

V_{zz} (a_0^{-3})	V_{yy} (a_0^{-3})	V_{xx} (a_0^{-3})	η	$\Delta EQ(mm/s)$ (calculated)^b	$\lvert\Delta EQ\rvert(mm/s)$ (experiment)^a
0.439	-0.311	-0.128	0.416	+0.73	0.62

Magnetic hyperfine field

	$\Delta\rho(0)$ (a_0^{-3})	H_c (kG)
1s-3s	-0.906	-474
valence	+0.077	+40
Total	-0.829	-434

a) From reference [84].

b) Q (^{57}Fe) = 0.16b (from ref. [91]).

Table II – Cartesian coordinates (Å) of nearest neighbor ligands to Ru^{VI} in [Ru(O)PHAB]

atom	x	y	z
O1	−1.296	−1.018	0.426
O2	0.565	1.276	1.285
O3	−0.953	1.393	−1.086
N1	0.768	−0.496	−1.672
N2	1.579	−0.981	0.676

Table III - Net Mulliken populations for Ru and ligand atomic charges in [Ru(O)PHAB] for 6 (embedded), 20 and 36 (naked) atom fragments, and the entire (66 atom) complex. Net charge = 0 for each fragment.

	6 atoms	20 atoms	36 atoms	entire
Ru 4d	5.63	5.78	5.74	5.74
5s	0.06	0.11	0.10	0.06
5p	0.13	0.23	0.25	0.15
net	2.19	1.87	1.90	2.04
O1				
net	-0.44	-0.44	-0.43	-0.53
O2				
net	-0.52	-0.44	-0.45	-0.63
O3				
net	-0.46	-0.52	-0.56	-0.42
N1				
net	-0.38	-0.39	-0.44	-0.63
N2				
net	-0.40	-0.39	-0.53	-0.44

Table IV – Mulliken populations , charges and bond orders from non-relativistic and relativistic calculations for $[Ir(CN)_5]^{3-}$. Ax and eq stand for axial and equatorial ligands, respectively.

Populations and Charges

Nonrelativistic			Relativistic			
Ir	5s	1.94	Ir	$5s_{1/2}$	1.96	
Populations	5p	5.91	Populations	$5p_{1/2}$	1.98	
	5d	7.43		$5p_{3/2}$	3.94	5p 5.92
	6s	0.09		$5d_{3/2}$	3.17	
	6p	0.45		$5d_{5/2}$	4.21	5d 7.38
				$6s_{1/2}$	0.23	
Charges	Ir	+1.18		$6p_{1/2}$	0.19	
	C_{ax}	+0.07		$6p_{3/2}$	0.32	6p 0.51
	N_{ax}	-0.85				
	C_{eq}	+0.02				
	N_{eq}	-0.87	Charges	Ir	+1.01	
				C_{ax}	+0.08	
				N_{ax}	-0.84	
				C_{eq}	+0.05	
				N_{eq}	-0.86	

Bond orders

	Nonrelativistic	Relativistic
Ir–C_{ax}	0.30	0.48
Ir –C_{eq} (each)	0.31	0.48
C_{ax}–N_{ax}	1.36	1.36
C_{eq}–N_{eq} (each)	1.31	1.31

Table V – Self-consistent Mulliken populations in NR and R models of a W_6 cluster.

Orbital		Nonrelativistic	Relativistic
5d	3/2	4.94	2.07
	5/2		2.22
6s		0.54	0.72
6p	1/2	0.55	0.30
	3/2		0.73

Table VI – Mulliken atomic orbital populations and net charges for $[W_6X^i_8X^a_6]^{2-}$ complexes from DV calculations. NR is nonrelativistic model; R is relativistic. Angular momentum subshells *j*=1/2, 3/2, 5/2 and an extended ligand basis set of valence ns, np, nd and (n+1)s optimized functions are indicated.

Orbital			Chloride		Bromide		Iodide	
			NR	R	NR	R	NR	R
W	5d	3/2	4.66	1.65	4.77	1.87	4.82	1.94
		5/2		1.76		1.93		2.00
	6s	1/2	0.02	0.62	0.08	0.87	0.14	0.87
	6p	1/2	0.28	0.17	0.25	0.24	0.33	0.26
		3/2		-0.06		0.02		0.09
		charge	1.07	2.10	0.94	1.21	0.75	0.96
X^i	s	1/2	1.97	2.03	1.97	2.03	1.96	2.02
	p	1/2	5.48	1.81	5.42	1.82	5.32	1.85
		3/2		3.60		3.52		3.42
	d	3/2	0.08	0.22	0.07	0.05	0.09	0.04
		5/2		0.29		0.08		0.07
	s*	1/2		0.22		0.21		0.15
		charge	-0.55	-1.16	-0.48	-0.70	-0.38	-0.55
X^a	s	1/2	1.98	2.03	1.99	2.01	1.97	2.00
	p	1/2	5.68	1.88	5.64	1.87	5.59	1.92
		3/2		3.68		3.56		3.48
	d	3/2	0.02	0.08	0.01	0.04	0.02	0.05
		5/2		0.12		0.06		0.06
	s*	1/2	0.01	0.09	0.01	0.08		0.06
		charge	-0.68	-0.87	-0.70	-0.61	-0.55	-0.56

Table VII – Comparison of symmetry type and gap (eV) between valence and conduction bands for $[W_6X_8^iX_6^a]^{2-}$ clusters, together with experimental emission and absorption bands.

Species	Method	HOMO	LUMO	VB-CB Gap
Chloride				
	NR[a]	t_{2u}	e_u	2.7
	R[b]	γ_{8u}	$\gamma_{8u},\gamma_{8u}^e$	2.8
	absorption[c]			2.5
	emission[d]			1.83
Bromide				
	NR	t_{2u}	t_{2u}	2.1
	R	γ_{8g}	γ_{7u}	2.7
	emission			1.85
Iodide				
	NR	t_{1g}	t_{2u}	2.0
	R	γ_{8g}	γ_{7u}	1.1
	emission			2.05

a) Gap=HOMO–LUMO energy.

b) HOMO and LUMO lie within VB, gap=VB peak to CB peak, see text.

c) Absorption edge of $(Bu_4N)_2Mo_6Cl_{14}$ in PMMC.

d) Emission band maximum.

e) Degenerate levels.

Table VIII - Mulliken populations and net atomic charges in cluster models of *annite*. Si_p and Fe_p indicate atoms in groups at periphery of cluster.

		$[RO_4(OH)_2]$	$[R(Si_4O_{14})(OH)_2]$		$[RO_4]$	$[R(SiFe)_3O_4]$	$[RO_4]$	$[R(SiFe)_3O_4]$
		R=Fe			R=Al		R=Si	
Cluster charge		-8.0	-12.0		-5.0	+13.0	-4.0	+14.0
	3d	6.00	5.98	3s	0.04	0.01	0.21	0.22
R	4s	0.13	0.06	3p	0.12	0.08	0.43	0.45
	4p	0.10	0.06		+2.84	+2.91	+3.36	+3.33
		+1.77	+1.90					
O_H	2s	1.94	1.95					
	2p	5.70	5.84					
		-1.64	-1.79					
O_{TO}	2s	2.00	1.95		1.98	1.95	1.96	1.90
	2p	5.93	5.81		5.88	5.69	5.87	5.72
		-1.93	-1.76		-1.86	-1.64	-1.83	-1.62
O_{TT}	2s		1.96		2.00	1.97	1.97	1.94
	2p		5.83		5.98	5.42	5.87	5.54
			-1.79		-1.98	-1.39	-1.84	-1.48
H	1s	0.38	0.22					
		+0.62	+0.78					
Si_p	3s		0.20			0.51		0.48
	3p		0.50			0.18		0.13
			+3.30			+3.31		+3.39
Fe_p	3d					5.44		5.49
	4s					0.49		0.26
	4p					0.08		0.05
						+1.99		+2.20

Table IX – Charge density $\rho_c(0)$ at the nucleus and Isomer Shift δ, Electric Field Gradient tensor, contact spin density $\rho_s(0)$, Magnetic Dipolar Field tensor, and net magnetic field H_F at iron site in *annite*. Results are given for clusters containing only first, and first plus second coordination shells about iron. Principal values and directions of principal axes (in parentheses) are given for EFG and dipolar field. The ^{57}Fe nuclear quadrupole moment is taken as 0.16 barn [91].

			$FeO_4(OH)_2$	$Fe(Si_4O_{14})(OH)_2$
$\rho_c(0)^a$				
3s	shallow core		140.53	140.02
	valence		1.66	1.90
			142.19	141.92
4s	valence		0.50	0.41
	TOTAL		142.69	142.33
δ(mm/s)^b			+1.15	+1.23
			EFG tensor(a_0^{-3})	
		V_{xx}	+1.10	-0.01
			(1.0,0.0,0.0)	(0.0,1.0,0.0)
		V_{yy}	+1.74	-2.35
			(0.0,1.0,0.0)	(0.0,0.0,1.0)
		V_{zz}	-2.84	+2.36
			(0.0,0.0,1.0)	(1.0,0.0,0.0)
η			0.23	0.99
ΔEQ(mm/s)			-4.59	+3.81
$\rho_s(0)^a$				
	core		-1.59	-1.60
	shallow core		+0.77	+0.77
	valence		+0.04	+0.14
	TOTAL		-0.78	-0.69
H_D tensor (a_o^{-3})		M_{xx}	+1.15	-0.13
			(1.0,0.0,0.0)	(0.0,1.0,0.0)
		M_{yy}	+1.75	-2.37
			(0.0,1.0,0.0)	(0.0,0.0,1.0)
		M_{zz}	-2.89	+2.48
			(0.0,0.0,1.0)	(1.0,0.0,0.0)
H_c(kOe)			-411	-362
H_D(kOe)			-181	+151
H_F(kOe)			-592	-211

^{a}In units of a_0^{-3}. ^{b}Related to α iron.

References

[1] T.H. Dunning, Jr. and P.J. Hay, in "Methods of Electronic Structure Theory", Ch. 1, ed. H.F. Schaefer III, (Plenum Press, New York, 1977).

[2] W.J. Hehre, L. Random, P. Schleyer and J.A. Pople, "Ab Initio Molecular Orbital Theory", (John Wiley & Sons, New York, 1986).

[3] S. Huzinaga, M. Klobukowski and Y. Sakai, J. Phys. Chem. **88**, 4880 (1984).

[4] P.J. Hay and W.R. Wadt, J. Chem. Phys. **82**, 270, 284, 299 (1985).

[5] For example: I. Shim and K.A. Gingerich, in "Physics and Chemistry of Small Clusters", P. Jena, B.K. Rao and S.N. Khanna, editors, (Plenum, New York, 1987) p. 523.

[6] J. Cized, J. Chem. Phys. **45**, 4256 (1966).

[7] R.J. Bartlett, J. Phys. Chem. **93**, 1697 (1989).

[8] R.G. Parr and W. Yang, "Density Functional Theory of Atoms and Molecules", Oxford University Press, New York (1989).

[9] E.S. Kryachko and E. Ludena, "Density Functional Theory of Many-Electron Systems", Kluwer Academic, Dordrecht (1990).

[10] J. Callaway and N.H. March, in "Solid State Physics", ed. H. Ehrenreich and D. Turnbull, Academic, New York (1984).

[11] "Density Functional Methods in Chemistry", J.K. Labanowski and J.W. Andzelm, editors, (Springer-Verlag, Berlin, 1991).

[12] "Density Functional Theory of Molecules, Clusters, and Solids", D.E. Ellis, editor, (Kluwer Academic, Dordrecht, 1995).

[13] J.P. Perdew, Phys. Rev. B**33**, 8822 (1986); ibid B**34**, 7406 (1986).

[14] See, for example: J. Callaway, "Energy Band Theory", "Pure and Applied Physics" monograph no. 16, Academic Press, New York (1964).

[15] D.E. Ellis and G.S. Painter, Phys. Rev. B2, 2887 (1970).

[16] D.E. Ellis and J. Guo, in "Electronic Density Functional Theory of Molecules, Clusters and Solids", ed. D.E. Ellis, Kluwer, Dordrecht (1995) p. 263.

[17] A. Rosen and D.E. Ellis, J. Chem. Phys. **62**, 3039 (1975).

[18] D.E. Ellis, in "Actinides in Perspective", edited by N.M. Edelstein (Pergammon, New York, 1992) p. 123.

[19] A.D. Becke, Phys. Rev. A**38**, 3098 (1988).

[20] P. Hohenberg and W. Kohn, Phys. Rev. **136**, B847 (1964); W. Kohn and L.J. Sham, Phys. Rev. **137**, A1697 (1965); W. Kohn and L.J. Sham, Phys. Rev. **140**, A1133 (1965).

[21] G.S. Painter and D.E. Ellis in "Computational Methods in Band Theory", Plenum, N. York (1971), pg. 271 and 277.

[22] G.S. Painter and D.E. Ellis, Phys. Rev. B **1**, 4747 (1970).

[23] D.E. Ellis and F.W. Averill, J. Chem. Phys. **60**, 2856 (1974).

[24] E.J. Baerends, D.E. Ellis and P. Ros, Chem. Phys. **2**, 41 (1973).

[25] A. Rósen, D.E. Ellis, H. Adachi and F.W. Averill, J. Chem. Phys. **65**, 3629 (1976).

[26] C.B. Haselgrove, Math. Comp. **15**, 323 (1961).

[27] H. Conroy, J. Chem. Phys. **47**, 5307 (1967).

[28] D.E. Ellis, Int. J. Quant. Chem. **2S**, 35 (1968).

[29] A.H. Stroud, "Approximate calculation of multiple integrals", Prentice Hall, Englewood Cliffs, NJ (1971).

[30] F.L. Hirshfeld, Theor. Chim. Acta **44**, 129 (1977).

[31] A. Becke, J. Chem. Phys. **88**, 2547 (1988).

[32] R.S. Mulliken, J. Chem. Phys. **23**, 1833 (1955); ibid, 1841 (1955).

[33] C. Umrigar and D.E. Ellis, Phys. Rev. B **21**, 852 (1980).

[34] T.D. Bouman and G.L. Goodman, J. Chem. Phys. **56**, 2478 (1972).

[35] D.E. Ellis and G.L. Goodman, Int. J. Quant. Chem. **25**, 185 (1984).

[36] P.J. Hay and W.R. Wadt, J. Chem. Phys. **82**, 229 (1985); M. Boring and J.H. Wood, J. Chem. Phys. **71**, 32 (1979); **71**, 392 (1979).

[37] B. Delley and D.E. Ellis, J. Chem. Phys. **76**, 1949 (1982).

[38] J.D. Jackson, "Classical Electrodynamics", Wiley, N. York (1975).

[39] J.C. Slater, "The self-consistent field for molecules and solids", vol. 4, McGraw-Hill, New-York (1974).

[40] R. Gaspar, Acta Phys. Acad. Sci. Hung. **3**, 263 (1954).

[41] J.M. MacLaren, D.P. Clougherty, M.E. McHenry and M.M. Donovan, Computer Physics Communications **66**, 383 (1991), and references therein.

[42] S.H. Vosko, L. Wilk and M. Nusair, Can. J. Phys. **58**, 1200 (1980).

[43] D.M. Ceperley and B.J. Alder, Phys. Rev. Lett. **45**, 566 (1980); D. Ceperley, Phys. Rev. B **18**, 3126 (1978).

[44] C. Kittel, "Introduction to Solid State Physics", 7th. edition, J. Wiley, New York (1996), appendix B.

[45] B. Delley, D.E. Ellis, A.J. Freeman, E.J. Baerends and D. Post, Physical Review B **27**, 2132 (1983).

[46] P.K. Kowash and D.E. Ellis, Phys. Rev. B **39**, 1908 (1989).

[47] D. Guenzburger and D.E. Ellis, Phys. Rev. Letters **67**, 3832 (1991).

[48] D. Guenzburger and D.E. Ellis, Phys. Rev. B **45**, 285 (1992).

[49] H.A. Bethe and R.W. Jackson, "Intermediate Quantum Mechanis", McGraw-Hill, New York (1968);
M.E. Rose, "Relativistic Effects in Atoms, Molecules, and Solids", Plenum, New York (1983).

[50] I.P. Grant, Proc. Roy. Soc. London, Ser A **262**, 555 (1961);
R.D. Cowan and D.C. Griffin, J. Opt. Soc. Am. **66**, 1010 (1976);
J.-P. Desclaux and P. Pyykkö, Chem. Phys. Lett. **29**, 534 (1974);

P.J. Hay, W.R. Wadt, L.R. Kahn, and F.W. Bobrowicz, J. Chem. Phys. **69**, 984 (1978).

[51] T. Ziegler, J.G. Snijders and E.J. Baerends, J. Chem. Phys. **74**, 1271 (1981).

[52] B.X. Xu, A.K. Rajagopal, and M.V. Ramana, J. Phys. C, **17**, 1339 (1984);
M. Vijayakumar, N. Vaidehi, and M.S. Gopinathan, Phys. Rev. **A40**, 6834 (1989).

[53] D.E. Ellis, J. Phys. B **10**, 1 (1977) and references therein.

[54] D.D. Koelling and A.H. MacDonald, in "Relativistic Effects in Atoms, Molecules, and Solids", G.L. Malli, ed., Plenum, New York (1983), p. 227.

[55] S.R. Nogueira and D. Guenzburger, Int. J. Quant. Chem. **57**, 471 (1996).
D.E. Ellis, in "Actinides in Perspective", N.M. Edelstein, ed., Pergamon, New York (1982), p. 123;
C.Y. Yang, J. Chem. Phys. **68**, 2626 (1978).

[56] D.A. Liberman, J.T. Waber, and D.T. Cromer, Phys. Rev. **A27**, 137 (1965);
P. Pyykkö and J.-P. Desclaux, Acct. Chem. Res. **12**, 276 (1979);
M. Pepper and B.E. Bursten, Chem. Rev. **91**, 719 (1991).

[57] D.E. Ellis, Int. J. Quantum Chem. Symp. **11**, 201 (1977);
D.E. Ellis, in "Handbook on the Physics and Chemistry of the Actinides", A.J. Freeman and G.H. Lander, eds., North-Holland, Amsterdam (1985), p. 1.

[58] M. Tinkham, "Group Theory and Quantum Mechanics", McGraw-Hill, New York (1964).

[59] H. Wilkinson, "The Algebraic Eigenvalue Problem", Clarendon Press, Oxford (1965).

[60] A. Berces and T. Ziegler, Topics in Curr. Chem. **182**, 41 (1996).

[61] G.A. Benesh and D. Gebreselasie, Phys. Rev. **B54**, 5940 (1996).

[62] P.E. Gill, W. Murray, and M.H. Wright, "Practical Optimization", Academic, London (1981).

[63] R. Carr and M. Parinello, Phys. Rev. Lett. **55**, 247 (1985);
R. Car and M. Parinello, in "Simple Molecular Systems at Very High Density", A. Polian, P. Loubeyre and N. Boccara, eds., Plenum, New York (1989); P.J. Kelley and R. Car, Phys. Rev. **B45**, 6543 (1992).

[64] S. Kirkpatrick, C.D. Gelat, and M.P. Vecchi, Science **220**, 671 (1983);
S. Kirkpatrick, J. Stat. Phys. **34**, 975 (1984);
E.P.G. Arêas, P.G. Pascutti, S. Schreier, K.C. Mundim, and P.M. Bisch, J. Phys. Chem. **99**, 14882 (1995);
F. Yonezawa, ed., "Molecular Dynamics Simulations", Springer-Verlag, Berlin, (1992).

[65] J.F. Lutsko, D. Wolf, S. Yip, S.P. Philpott, and T. Nguyen, Phys. Rev. **B38**, 2887 (1988).

[66] R.W. Grimes, C.R.A. Catlow, and A.L. Shluger, eds., "Quantum Mechanical Calculations in Solid State Studies", World Scientific, Singapore (1992).

[67] GROMOS: Gröningen Molecular Simulation Data Base, developed at Gröningen University.

[68] M.S. Daw and M.I. Baskes, Phys. Rev.. **B29**, 6443 (1984);
S.M.. Foiles, M.I. Baskes, and M.S. Daw, Phys. Rev. **B33**, 7983 (1986).

[69] C.R.A. Catlow, I.D. Faux and M.J. Norgett, J. Phys. C **9**, 419 (1976).

[70] L. Guo, D.E. Ellis, K.C. Mundim and B.M. Hoffman, submitted.

[71] J.R. Ferraro, Coord. Chem. Rev. **43**, 205 (1982);
J. Martinsen, R.I. Green, S.M. Palmer and B.M. Hoffman, J. Am.. Chem. Soc. **105**, 677 (1983);
L.J. Pace, J. Martinsen, A. Ulman, B.M. Hoffman and J.A. Ibers, J. Am. Chem. Soc. **105**, 2612 (1983);
T.P. Newcomb, M.R. Godfrey, B.M. Hoffman and J.A. Ibers, Inorg. Chem. **29**, 223 (1990);
M.Y. Ogawa, S.M. Palmer, K. Liou, G. Quiron, J.A. Thompson, M. Poirier and B.M. Hoffman, Phys. Rev. B **39**, 682 (1989); M.Y. Ogawa, J. Martinsen, S.M. Palmer, J.L. Stanton, J. Tanaka, R.L. Greene, B.M. Hoffman and J.A. Ibers J. Am. Chem. Soc. **109**, 1115 (1987).

[72] L. Guo, D.E. Ellis, B.M. Hoffman and Y. Ishikawa, Inorg. Chem. **35**, 5304 (1996).

[73] A. Rosa and E.J. Baerends, Inorg. Chem. **31**, 4717 (1992); **32**, 5637 (1993); **33**, 584 (1994).

[74] B.C. Wiegand and C.M. Friend, Chem. Revs. **92**, 491 (1992).

[75] R.A. Sánchez-Delgado, J. Mol. Catal. **86**, 287 (1994), and references therein.

[76] B.A. Sexton, Surf. Sci. **163**, 99 (1985).

[77] L. Rincón, J. Terra, D. Guenzburger and R.A. Sánchez-Delgado, Organometallics **14**, 1292 (1995).

[78] D.D. Awschalom and D.P. DiVincenzo, Physics Today **48**, 43 (1995).

[79] D.D. Awschalom, D.P. DiVincenzo and J.F. Smyth, Science **258**, 414 (1992).

[80] G.C. Papaefthymiou, Phys. Rev. B **46**, 10366 (1992).

[81] D.D. Awschalom, J.F. Smyth, G. Grinstein, D.P. DiVincenzo and D. Loss, Phys. Rev. Letters **68**, 3092 (1992).

[82] R.D. Michael, R.D. Schull, L.J. Swartzendruber, L.H. Bennett and R.E. Watson, J. Mag. Mag. Mat. **111**, 29 (1992); R. Sessoli, D. Gatteschi, A. Caneschi and M.A. Novak, Nature **365**, 141 (1993).

[83] D. Gatteschi, E. Sessoli, W. Plass, A. Müller, E. Krickemeyer, J. Meyer, S. Sölter and P. Adler, Inorg. Chem. **35**, 1926 (1996).

[84] K.L. Taft, C.D. Delfs, G.C. Papaefthymiou, S. Foner, D. Gatteschi and S.J. Lippard, J. Am. Chem. Soc. **116**, 823 (1994).

[85] Z. Zeng, Y. Duan and D. Guenzburger, Phys. Rev. B, in press.

[86] N.N. Greenwood and R.C. Gibb, "Mössbauer Spectroscopy", Chapman and Hall, London (1971).

[87] J. Terra and D. Guenzburger, J. Phys. Chem. **99**, 4935 (1995).

[88] D. Guenzburger and D.E. Ellis, Phys. Rev. B **22**, 4203 (1980).

[89] J. Terra and D. Guenzburger, Phys. Rev. B **44**, 8584 (1991).

[90] D. Guenzburger and D.E. Ellis, Phys. Rev. B **36**, 6971 (1987).

[91] P. Dufek, P. Blaha and K. Schwarz, Phys. Rev. Letters **75**, 3545 (1995).

[92] R.H. Holm, Chem. Rev. **87**, 1401 (1987).

[93] S. Alexander, J.L. Séris, and B. Meunier, Science **268**, 1163 (1995); R.A. Sheldon, and J.A. Kochi, *Metal-Catalyzed Oxidation of Organic Compounds*, Academic Press, New York (1981).

[94] N.L.P. Fackler, S.S. Zhang, and T.V. O'Halloran, J. Am. Chem. Soc. **118**, 481 (1996).

[95] A.R. Rossi and R. Hoffmann, Inorg. Chem. **14**, 365 (1975).

[96] F.K. Winkler and J.D. Dunitz, J. Mol. Biol. **59**, 169 (1971); F.C. Anson, T.J. Collins, S.L. Gipson, J.T. Keech, T.E. Kraft and G.T. Peake, J. Am. Chem. Soc. **108**, 6593 (1986).

[97] D.E. Ellis, N.F.L. Fackler, and T.V. O'Halloran, submitted.

[98] N.V. Vugman, R.P.A. Muniz and J. Danon, J. Chem. Phys. **57**, 1297 (1972).

[99] S.R. Nogueira and D. Guenzburger, Int. J. Quant. Chem. **57**, 471 (1996).

[100] T.C. Zietlow, W.P. Schaefer, B. Sadeghi, N. Hua, and H.B. Gray, Inorg. Chem. **25**, 2195 (1986).

[101] R. Bain, D.E. Ellis, L.M. Robinson, and D.F. Shriver, submitted.

[102] L.M. Robinson, R. Bain, D.F. Shriver and D.E. Ellis, Inorg. Chem. **34**, 5588 (1995).

[103] T.C. Zietlow, M.D. Hopkins and H.B. Gray, J. Solid State Chem. **57**, 112 (1985); T.C. Zietlow, D.G. Nocera and H.B. Gray, Inorg. Chem. **25**, 1351 (1986).

[104] B.K. Cho, P.C. Canfield, L.L. Miller, D.C. Johnston, W.P. Beyermann, and A. Yatskar, Phys. Rev. **B52**, 3684 (1995) and references therein.

[105] W.E. Pickett and D.J. Singh, Phys. Rev. Letters **72**, 3702 (1994);
L.F. Mattheiss, Phys. Rev. **B49**, 13279 (1994).

[106] E. Johnston-Halperin, J. Fiedler, D.E. Farrel, M. Xu, K. Cho, P.C. Canfield, D.K. Finnemore, and D.C. Johnston, Phys. Rev. **B51**, 12852 (1995).

[107] B.K. Cho, M. Xu, P.C. Canfield, L.L. Miller, and D.C. Johnston, Phys. Rev. **B52**, 3676 (1995).

[108] A.I. Goldman, C. Stassis, P.C. Canfield, J. Zarestky, P. Dervenagas, B.K. Cho, D.C. Johnston and B. Sterlieb, Phys. Rev. **B50**, 9668 (1994);
Z. Zarestky, C. Stassis, A.I. Goldman, P.C. Canfield, P. Dervenagas, B.K. Cho, and D.C. Johnston, Phys. Rev. **B51**, 678 (1995).

[109] Z. Zeng, D.E. Ellis, D. Guenzburger, and E.M. Baggio-Saitovitch, Phys. Rev. **B53**, 6613 (1996).

[110] Z. Zeng, D.R. Sanchez, D. Guenzburger, D.E. Ellis, E.M. Baggio-Saitovitch, and H. Micklitz, Phys. Rev. **B55**, xxxx (1997).

[111] Z. Zeng, D. Guenzburger, D.E. Ellis and E.M. Baggio-Saitovitch, Physica C **271**, 23 (1996); Z. Zeng, D.E. Ellis, D. Guenzburger and E.M. Baggio-Saitovitch, Phys. Rev. B **54**, 13020 (1996).

[112] G.Y. Guo and W.M. Temerman, Phys. Rev. **B41**, 6372 (1990).

[113] T. Ezawa, W.A.A. Macedo, U. Glos, W. Keune, K.P. Schletz and U. Kirchbaum, Physica B **161**, 281 (1989), and references therein.

[114] W. Keune, T. Ezawa, W.A.A. Macedo, U. Glos and K.P. Schletz, Physica B **161**, 269 (1989), and references therein.

[115] J. Kübler, Phys. Lett. **81A**, 81 (1981); C.S. Wang, B.M. Klein and H. Krakauer, Phys. Rev. Lett. **54**, 1852 (1985).

[116] E.F. Wassermann, Phys. Scr. **T25**, 209 (1989).

[117] D. Guenzburger and D.E. Ellis, Phys. Rev. B **51**, 12519 (1995).

[118] D. Guenzburger and D.E. Ellis, Phys. Rev. B **52**, 13390 (1995).

[119] H. Chacham, E. Galvão da Silva, D. Guenzburger and D.E. Ellis, Phys. Rev. B **35**, 1602 (1987).

[120] J.A. Tossel and G.V. Gibbs, Phys. Chem. Mineral **2**, 21 (1977).
G.V. Gibbs, Am. Mineral. **67**, 421 (1982);
J. Sauer, J. Chem. Rev. **89**, 199 (1989);
A.C. Lasaga, Rev. Mineral. **23**, 17 (1990);
B.J. Teppen, D.M. Miller, S.Q. Newton and L. Schäfer, J. Phys. Chem. **98**, 12545 (1994);

H.V. Brand, L.A. Curtiss and L.E. Iton, J. Phys. Chem. **96**, 7725 (1992);
D.H. Sherman, Phys. Chem. Minerals **14**, 355 (1987); **14**, 364 (1987); Ame. Mineral. **75**, 256 (1990).

[121] R. Dovesi, C. Pisani, C. Roetti and B. Silvi, J. Chem. Phys. **86**, 6967 (1987);
A.C. Hess and V.R. Saunders, J. Phys. Chem. **96**, 4367 (1992); J.C. White and A.C. Hess, J. Phys. Chem. **97**, 6398 (1993); **97**, 8703 (1993);
Yong-nian Xu and W.Y. Ching, Phys. Rev. **B44**, 11048 (1991).

[122] J. Terra and D.E. Ellis, Proc. Latin Amer. Conf. Möss. Effect, 1996, to be published.

[123] R.W.G. Wyckoff, *Crystal Structures*, Wiley, New York, (1968) vol. 4.

[124] G.J. Redhamer, A. Beran, E. Dachs and G. Amthauer, Phys. Chem. Minerals **20**, 382 (1993).
D.G. Rancourt, I.A.D. Christie, M. Royer, H. Kodama, J.-L. Robert, A.E. Lalonde and E. Murad, Am. Mineral **79**, 51 (1994);
D.G. Rancourt, Phys. Chem. Minerals **21**, 250 (1994);
D.G. Rancourt, J.Y. Ping and R.G. Berman, Phys. Chem. Minerals **21**, 258 (1994);
G.J. Redhamer, E. Dachs and G. Amthauer, Phys. Chem. Minerals **22**, 282 (1995);
D.G. Rancourt, J.Y. Ping, B. Boukili and J.-L. Robert, Phys. Chem. Minerals (in press).

[125] D.G. Rancourt, I.A.D. Christie, G. Lamarche, I.S. Swainson and S. Flandrois, J. Mag. Magnetic Mat. **138**, 31 (1994).

[126] V. Ravikumar and V.P. Dravid, Ultramicros **52**, 557 (1993);
M.M. McGibbon, N.D. Browning, M.F. Chisholm, A.J. McGibbon, S.J. Pennycook, V. Ravikumar and V.P. Dravid, Science **266**, 102 (1994);
H. Gu, M. Ceh, S. Stemmer, H. Mullejans and M. Ruhle, Ultramicros. **59**, 215 (1995).

[127] V. Ravikumar, D. Wolf, and V.P. Dravid, submitted.

[128] R.P. Rodrigues, Ph.D thesis, Northwestern University, 1997;
R.P. Rodrigues, H.J. Chang, D.E. Ellis and V.P. Dravid, submitted.